Recalibration of the lunar chronology due to spatial cratering-rate variability

Anthony Lagain, Hadrien A. R. Devillepoix, Pierre Vernazza, Darrel Robertson, Mikael Granvik, Petr Pokorny, Anthony Ozerov, Patrick M. Shober, Laurent Jorda, Konstantinos Servis, et al.

Icarus 411 (2024) 115956

Contents lists available at ScienceDirect

Icarus

journal homepage: www.elsevier.com/locate/icarus

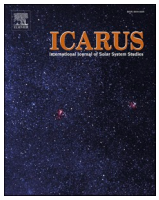

Recalibration of the lunar chronology due to spatial cratering-rate variability

Anthony Lagain [a,b,c,*], Hadrien A.R. Devillepoix [a,d], Pierre Vernazza [c,e], Darrel Robertson [f], Mikael Granvik [g,h], Petr Pokorny [i,j,k], Anthony Ozerov [l], Patrick M. Shober [m], Laurent Jorda [e], Konstantinos Servis [n], John H. Fairweather [a], Yoann Quesnel [b,c], Gretchen K. Benedix [a,o,p]

[a] Space Science and Technology Centre, School of Earth and Planetary Science, Curtin University, Perth, Australia
[b] Aix Marseille Univ., CNRS, IRD, INRA, CEREGE, Aix en Provence, France
[c] Aix-Marseille Univ., Institut ORIGINES, Marseille, France
[d] International Centre for Radio Astronomy Research, Curtin University, Perth, Australia
[e] Aix Marseille Univ., CNRS, CNES, Laboratoire d'Astrophysique de Marseille, Marseille, France
[f] NASA Ames Research Center, Moffett Field, CA, USA
[g] Department of Physics, University of Helsinki, Helsinki, Finland
[h] Asteroid Engineering Laboratory, Luleå University of Technology, Kiruna, Sweden
[i] Department of Physics, The Catholic University of America, Washington, DC 20064, USA
[j] Astrophysics Science Division, NASA Goddard Space Flight Center, Greenbelt, MD 20771, USA
[k] Center for Research and Exploration in Space Science and Technology, NASA/GSFC, Greenbelt, MD 20771, USA
[l] Columbia University, New York, NY, USA
[m] Institut de Mécanique Céleste et de Calcul des Éphémérides, Observatoire de Paris, 77 Av. Denfert-Rochereau, 75014 Paris, France
[n] Pawsey Supercomputing Centre, CSIRO, Kensington, WA, Australia
[o] Department of Earth and Planetary Sciences, Western Australian Museum, WA, Australia
[p] Planetary Sciences Institute, Tucson, AZ, USA

ARTICLE INFO

Keywords:
Moon
Impact craters
Impact flux
Chang'e 5
Chronology

ABSTRACT

Cratering chronologies are used to derive the history of planetary bodies and assume an isotropic flux of impactors over the entire surface of the Moon. The impactor population is largely dominated by near-Earth-objects (NEOs) since ~3.5 billion years ago. However, lunar impact probabilities from the currently known NEO population show an excess of impacts close to the poles compared to the equator as well as a latitudinal dependency of the approach angle of impactors. This is accompanied by a variation of the impact flux and speed with the distance from the apex due to the synchronicity of the lunar orbit around the Earth. Here, we compute the spatial dependency of the cratering rate produced by such variabilities and recalibrate the lunar chronology. We show that it allows to reconcile the crater density measured at mid-latitudes around the Chang'e-5 landing site with the age of the samples collected by this mission. Our updated chronology leads to differences in model ages of up to 30% compared to other chronology systems. The modeled cratering rate variability is then compared with the distribution of lunar craters younger than ~1 Ma, 1 Ga and 4 Ga. The general trend of the cratering distribution is consistent with the one obtained from dynamical models of NEOs, thus potentially reflecting a nonuniform distribution of orbital parameters of ancient impactor populations, beyond 3.5 Ga ago, i.e., planetary leftovers and cometary bodies. If the nonuniformity of the cratering rate could be tested elsewhere in the Solar System, the recalibrated lunar chronology, corrected from spatial variations of the impact flux and approach conditions of impactors, could be extrapolated on other terrestrial bodies such as Mercury and Mars, at least over the last 3.5 billion years. The modeled cratering rate presented here has strong implications for interpreting results of the Artemis program, aiming to explore the South Pole of our satellite, in particular when it will come to link the radiometric age of the samples collected in this region and the crater density of the sampled units.

* Corresponding author at: Aix Marseille Univ., CNRS, IRD, INRA, CEREGE, Aix en Provence, France.
E-mail address: lagain@cerege.fr (A. Lagain).

https://doi.org/10.1016/j.icarus.2024.115956
Received 29 August 2023; Received in revised form 5 January 2024; Accepted 7 January 2024
Available online 9 January 2024

1. Introduction

Impact craters on planetary surfaces offer an extraordinary way to record temporal information of geological events having shaped their surface (Fassett, 2016). They also record impactor characteristics through both time and space (Neukum et al., 2001; Bottke et al., 2015). The knowledge of the impact-cratering flux on planetary bodies has been significantly improved since lunar samples have been radiometrically dated, thus allowing us to calibrate the cratering chronology of our satellite (Neukum et al., 2001; Bottke et al., 2015; Hartmann and Neukum, 2001). Subsequent works transposed lunar cratering models to other terrestrial surfaces such as Mars, Mercury, dwarf planets, and large asteroids (e.g., Le Feuvre and Wieczorek, 2011), providing a method to reconstruct their geological history along with the characteristics of impactor reservoirs (Fassett, 2016; Neukum et al., 2001; Bottke et al., 2015; Fassett and Thomson, 2014; Carr and Head III, 2010).

Most lunar chronology models currently used (Neukum, 1983; Hartmann and Neukum, 2001; Neukum et al., 2001; Marchi et al., 2009; Robbins, 2014) and recent recalibrations (Yue et al., 2022; Werner et al., 2023) assume an isotropic impact flux, and thus consider potential spatial variations of the impact flux and asteroid approach conditions (namely, the velocity and the angle of impacts) as negligible against other sources of uncertainties. Nevertheless, some works argue for significant spatial variations in the impact flux on lunar and inner planet surfaces (Le Feuvre and Wieczorek, 2011; Zahnle et al., 2001; Gallant et al., 2009; Morota et al., 2005; Le Feuvre and Wieczorek, 2008; Wang and Zhou, 2016). Specifically, the synchronous rotation of the Moon around the Earth causes a higher accumulation rate of impact craters and higher impact velocity at the apex of motion (0°N, 90°W) than at the antapex (0°N, 90°E). This effect is known and has been directly confirmed by seismic observations (Kawamura et al., 2011). Using a debiased model of the near-Earth-object (NEO) population (Bottke et al., 2002), Gallant et al. (2009) inferred that the crater production on the leading hemisphere is 1.28 times higher than on the trailing hemisphere. The theoretical cratering rate asymmetry is also enhanced by the relative impact velocity between the impactors and the Moon: the lunar orbital speed (1.022 km.s^{-1}) adds to the impactor heading towards the Moon and subtracts from the impactors chasing it (Wang and Zhou, 2016). This points to larger craters formed at the apex of motion compared to the antapex. Based on the orbital distribution of NEOs known two decades ago (Bottke et al., 2002), the modeling of the lunar cratering rate has also shown a variation in latitude, with an excess of ~10% at the equator compared to polar regions (Gallant et al., 2009; Le Feuvre and Wieczorek, 2008). This latitudinal fluctuation of the impact flux has often been attributed to the high concentration of low-inclined impactors contained in the debiased NEO population (Bottke et al., 2002). Recent improvement has been made to debias the NEO population (Granvik et al., 2018) with absolute magnitude ranging between 17 and 25 (equivalent to an impactor diameter between ~1500 m and ~ 30 m, respectively). The contribution of some asteroid groups with high-inclination orbits (16°–34°) in Granvik's et al. catalog, such as the Hungaria group (1.7–2.1 AU), leads to significant changes in the orbital distribution and dynamical lifetime of NEOs compared to previous predictions (Bottke et al., 2002). Using a synthetic realization of the NEO population model (Granvik et al., 2018) and impact probabilities (Pokorný and Vokrouhlický, 2013), the computation of the impact flux probabilities on the Moon with respect to the latitude (Robertson et al., 2021, 2023) reveals that the flux of impacts is ~1.13 times greater to the poles than at the equator, and that impacts near the poles are steeper with an average impact angle of ~49° compared to ~44° on equatorial regions. Crater size being dependent on the vertical component of the impact speed, this latitudinal increase of the mean impact angle would cause the formation of larger craters at higher latitudes. However, Robertson et al. (2021, 2023) did not report any significant change in the impact velocity with the latitude, and no longitudinal change in the impact angle is expected (Gallant et al., 2009).

These flux and approach conditions spatial variations have consequences in the cratering rate used to infer model ages of lunar geological units and the history of our satellite. Compared to other samples collected on the Moon by Apollo and Luna mission (Stöffler and Ryder, 2001), the Chang'e-5 mission collected basalts from the farthest region from the equator and the closest from the apex of motion ever sampled. Basalts from Northern Oceanus Procellarum region (43°N, 52°W) were dated at 2.03 Ga old (Li et al., 2021), thus offering a new calibration point for the lunar chronology. However, previous attempts to recalibrate the lunar chronology model considered the impact cratering asymmetry on the Moon negligible (Yue et al., 2022).

The early bombardment in the Earth-Moon system was dominated by leftover planetesimals before the NEO population (mostly asteroids escaping from the main belt) took over ~3.5 Ga ago and produced most of the impacts since that time (Bottke et al., 2015; Morbidelli et al., 2018; Xie et al., 2021; Nesvorný et al., 2017, 2022). This change in the impactor population raises the question about the temporal validity of the latitudinal dependency of the impact flux inferred from the current NEO population (Robertson et al., 2021, 2023).

In this study, we compute the spatial variability of the cratering rate to correct each calibration point of the lunar chronology based on their location. We provide a comprehensive lunar chronology model, valid at specific coordinates on the surface, and compare it with previous chronologies. We evaluate the influence of the Earth-Moon distance variation over time in the asymmetry of the cratering rate (more specifically in the impact velocity and in the gravitational focusing of the Earth-Moon system). We finally analyze the distribution of lunar craters formed no later than ~1 Ma, ~1 Ga and ~ 4 Ga ago, in order to test the spatial variability of the cratering rate through geological timescale, and this, for periods dominated by NEO impactors (<3.5 Ga) and beyond, dominated by planetary leftovers and comet populations (Bottke et al., 2015; Morbidelli et al., 2018; Xie et al., 2021; Nesvorný et al., 2017, 2022). This work will allow to recalibrate the chronology of other planetary bodies such as Mercury and Mars, along with future interpretations of samples collected by NASA's Artemis missions to the lunar south polar region.

2. Methods

2.1. Computing the cratering rate asymmetry

We compute the spatial variability of the lunar cratering rate from the combination of the pole/equator asymmetry of the impact flux and impact angle derived from a model of the NEO population (Robertson et al., 2021, 2023), and the apex/antapex asymmetry of the flux and impact speed (Gallant et al., 2009; Wang and Zhou, 2016). The leading/trailing asymmetry of the cratering rate being mostly driven by the lunar orbit synchronicity and impact speed, there is no major difference between published NEO models. In other words, implementing the new population of NEOs (Granvik et al., 2018) in the calculation of the cratering rate will have negligeable effects compared to the one published in the past (Gallant et al., 2009; Wang and Zhou, 2016).

2.2. The latitudinal asymmetry

The relative impact flux latitudinal dependency (Robertson et al., 2021, 2023) can be approximated by a polynomial law as a function of the angular distance from the equator Λ (in degrees, where $\Lambda \in [0°,90°]$, $\Lambda = |\lambda|$, $\lambda \in [-90°,90°]$ being the latitude):

$$F_y(\Lambda) = 3.861 \times 10^{-11}\Lambda^5 - 4.449 \times 10^{-9}\Lambda^4 - 5.437 \times 10^{-7}\Lambda^3 + 7.355 \times 10^{-5}\Lambda^2 - 1.676 \times 10^{-4}\Lambda + 9.284 \times 10^{-1} \quad (1)$$

The extrapolation of Eq. 1 over the entire globe is shown on Fig. 1a.

The average impact angle variability with respect to the distance from the equator (Robertson et al., 2021, 2023) Λ can be approximated

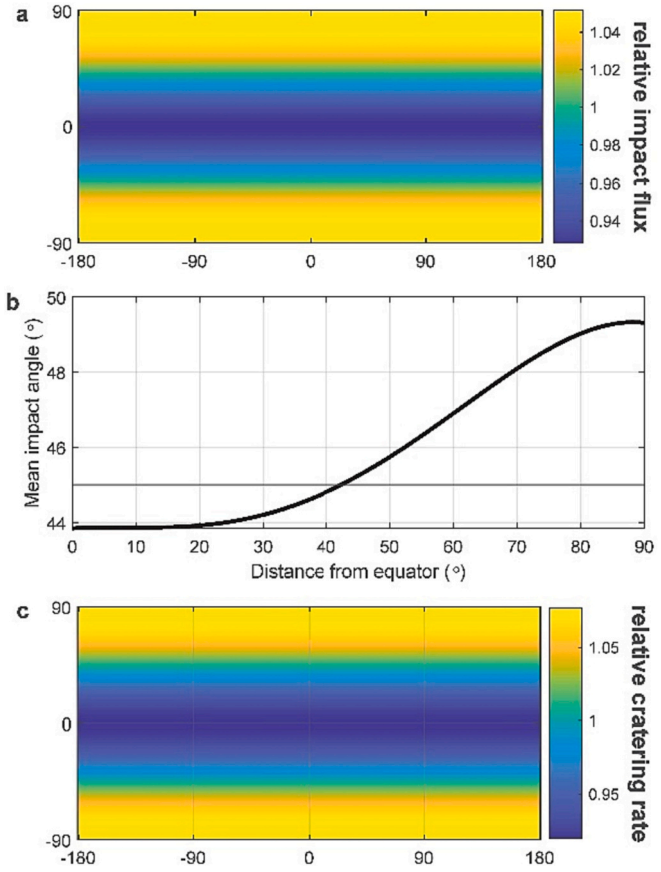

Fig. 1. Effect of the impact flux and approach conditions of NEOs on the latitudinal variation of the lunar cratering rate. a. Relative impact flux variation (Robertson et al., 2021, 2023). b. Mean impact angle fluctuation with respect to the distance from the equator (Robertson et al., 2021, 2023). c. Relative cratering rate latitudinal asymmetry obtained from the variation of the flux and impact angle with the latitude.

by a polynomial law (Fig. 1b):

$$\theta(\Lambda) = -4.056\times10^{-7}\Lambda^4 + 5.674\times10^{-5}\Lambda^3 - 1.251\times10^{-3}\Lambda^2 + 9.43\times10^{-3}\Lambda + 43.84 \quad (2)$$

Note that the results obtained by Robertson et al. (2021, 2023) and the subsequent approximation made here are not symmetric around 45° from the equator (Fig. 1b). The corresponding transient crater size at any angular distance from the equator Λ is computed independently from any variation of the impact speed V because impact probabilities of NEOs do not show any significant asymmetry of this parameter with the latitude (Robertson et al., 2021, 2023). It is chosen to be equal to 12 km. s^{-1} in the following equation:

$$D_t(\Lambda) = 1.161\times\left(\frac{\rho_i}{\rho_t}\right)^{1/3}\times L^{0.78}\times V^{0.44}\times g_{\mathbb{C}}{}^{-0.22}\times sin^{1/3}\theta(\lambda) \quad (3)$$

where ρ_i and ρ_t are respectively the density of the impactor taken as 1900 $kg.m^{-3}$ (the density of asteroid Itokawa, typical for small asteroids (Fujiwara et al., 2006; Carry, 2012)) and the target, 3000 $kg.m^{-3}$ (Archinal et al., 2015), L the impactor size, V the average impactor velocity at the surface, $g_{\mathbb{C}}$ the lunar gravitational acceleration, and θ, the impact angle. Note that the final crater size can be computed using a set of two scaling laws, each associated with a formation regime: strength or gravity-dominated (Collins et al., 2005). The choice of the scaling law to compute the final crater diameter (Eq. 3) is dependent on the simple to complex transition diameter, itself dependent on the impact angle and speed. The relative cratering rate Γ_y is thus slightly dependent on crater size. However, the difference between the final crater diameter D formed at the equator $D(\Lambda = 0°)$ and the final crater diameter formed at Λ, $D(\Lambda)$, is small: $\left|\frac{D(\Lambda=0°)}{D(\Lambda)} - 1\right| \ll 1$. Thus, the difference in the number of craters larger than D with respect to Λ is $\frac{N(D_{\Lambda=0°})}{N(D_\Lambda)} \approx 1 + b\left(\frac{D_\Lambda}{D_{\Lambda=0°}}\right) \approx \left(\frac{D_\Lambda}{D_{\Lambda=0°}}\right)^b$, where $b = -\frac{D}{N}\times\frac{dN}{dD}$. In other words, b is the logarithmic slope of the production function, which varies from ~1.3 to ~3.2 on the Moon (e.g., Neukum et al., 2001; Minton et al., 2019), depending on crater size and crater accumulation rate (Minton et al., 2019). The final diameter D being proportional to the transient diameter D_t, then the relative cratering rate Γ_y can be written:

$$\Gamma_y(\Lambda) = F_y(\Lambda)\times\left(\frac{D_t(\Lambda)}{D_t(\Lambda=0°)}\right)^b \quad (4)$$

This consideration leads to a crater size dependency on Γ_y when $b \neq 1$. In the present study, we will consider b equal to 3.2 (Neukum et al., 2001), the typical slope of the crater production function for $D < 4$ km. The relative cratering rate variation with the latitude is shown on Fig. 1c.

2.3. The leading/trailing hemisphere asymmetry

The leading/trailing hemisphere asymmetry of the relative impact flux is described as a function of the angular distance from the apex Φ (Gallant et al., 2009) and can be written:

$$F_x(\Phi) = 9.98\times10^{-1}\left(1 + 4.64\times10^{-2}\times cos\Phi\right)^{2.812} \quad (5)$$

where $\Phi \in [0°, 180°]$ and is dependent in both latitudes λ and longitudes φ (in radians):

$$\Phi = arccos\left(-cos(\lambda)sin(\varphi)\right) \quad (6)$$

The variation of the flux over the entire globe is shown in Fig. 2a.

The impact velocity V as a function of the angular distance from the apex Φ is computed using analytical expressions from Wang and Zhou (2016), assuming a vertical impact at the surface (Fig. 2b):

$$V(\Phi) = \frac{I_1}{I_0} \quad (7)$$

where

$$I_0 = 2V_{av}(sin\sigma - \sigma cos\sigma), \quad (8)$$

$$I_1 = V_{av}{}^2\left[\left(1 + 2cos^2\sigma\right)\sigma - 3sin\sigma cos\sigma\right], \quad (9)$$

$$\sigma = arccos\left(\frac{V_{\mathbb{C}}}{V_{av}}sin\varphi\right), \quad (10)$$

With $V_{\mathbb{C}}$ is the orbital speed of the Moon, V_{av} the average impact velocity on the Moon, 12 $km.s^{-1}$ (V in Eq. 3) and φ is the longitude.

The transient crater size formed at any distance from the apex Φ can be written (Collins et al. (2005):

$$D_t(\Phi) = 1.161\times\left(\frac{\rho_i}{\rho_t}\right)^{1/3}\times L^{0.78}\times V(\Phi)^{0.44}\times g_{\mathbb{C}}{}^{-0.22}\times sin^{1/3}\theta, \quad (11)$$

Note that here, the impact angle θ is considered constant across the longitudes, and equal to the average impact angle, i.e., 45° (the average of $sin^{1/3}\theta$ differing by 5% from the average impact angle, the non-linearity of this parameter in the scaling law is considered negligible in the choice of the impact angle). The relative cratering rate Γ_x (Fig. 2c) is thus function of the impact flux and the transient crater diameter D_t:

$$\Gamma_x(\Phi) = F_x(\Phi)\times\left(\frac{D_t(\Phi)}{D_t(\Phi=90°)}\right)^b, \quad (12)$$

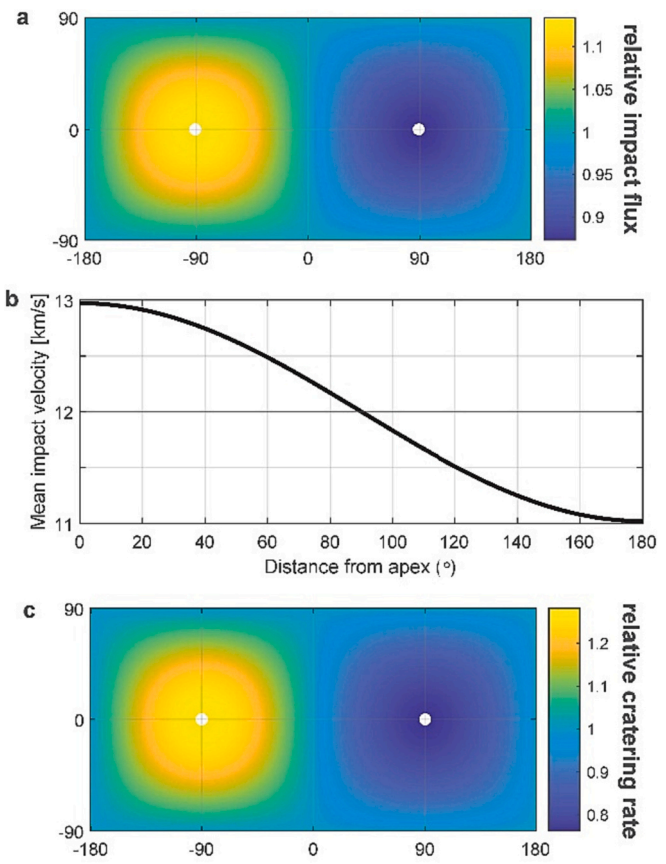

Fig. 2. Effect of the impact flux and approach conditions of NEOs on the variation of the lunar cratering rate with respect to the distance from the apex. a. Relative impact flux variation (Gallant et al., 2009). b. Mean impact velocity with respect to the distance from the apex (Wang and Zhou, 2016). c. Relative cratering rate asymmetry between the leading and trailing hemisphere obtained from the variation of the flux and impact velocity with the distance from the apex of motion. White dots on panels a and c correspond to the apex and the antapex.

2.4. Combination of spatial dependencies in the cratering rate

The combination of effects shown in Figs. 1 and 2 allows to compute the relative cratering rate fluctuation shown in Fig. 3 and provided in Dataset S1. For convenience, we give the analytical solution of the relative cratering rate as a function of the latitude and longitude (in radian), described as a trigonometric polynomial of the form:

$$\Gamma(\varphi,\lambda) = -1.616\times10^{-2}sin\varphi + 1.477cos\lambda + 1.189\times10^{-2}sin^2\varphi - 8.096\times10^{-1}cos^2\lambda - 2.268\times10^{-1}sin\varphi\cos\lambda - 5.143\times10^{-4}sin^3\varphi + 2.361cos^3\lambda + 1.041\times10^{-8}\varphi^2 + 4.568\times10^{-1}\lambda^2, \quad (13)$$

The coefficient of determination R^2 is 0.9983.

The polar impact flux (Robertson et al., 2021, 2023) (Fig. 1a) is enhanced by ~13% compared to the equator. Accounting for the impact angle variability shown in Fig. 1b leads to a pole/equator ratio of ~1.26 (Fig. 1c). As for the variation with the distance from the apex, the lunar synchronous rotation leads to an enhancement of the flux by ~30% at the apex of motion compared to the antapex (Gallant et al., 2009) (Fig. 2a). The apex/antapex cratering rate ratio obtained by accounting for the variability of the encounter impact speed (Fig. 2b, Wang and Zhou, 2016) is ~1.68 (Fig. 2c).

All these effects considered, the minimum of the relative cratering rate is naturally at the antapex of motion (~0.69), while the maximum, which results from the competition between the apex/antapex asymmetry and the latitudinal effect, is located at ±60°N, 90°W (~1.22). The ratio of the maximum and minimum of the relative cratering rate (Fig. 3) is 1.77.

2.5. The crater density associated with Chang'e-5 samples

The crater density N for D > 1 km, denoted $N(1)$, associated with the age of lunar samples offered a way to calibrate the lunar chronology and derive model ages of the surface.

The basalts recently collected on Oceanus Procellarum by the Chang'e-5 mission are the only lunar samples that can constrain the chronology between ~3 Ga and ~800 Ma (Li et al., 2021). Different studies report a variety of Crater-Size Frequency Distributions (CSFDs) and $N(1)$ values measured on different terrains surrounding the Chang'e-5 collection site (Jia et al., 2020; Williams et al., 2018; Qian et al., 2021; Giguere et al., 2022). As recently discussed by Giguere et al. (2022), crater density discrepancies measured on overlapped areas between different studies can be partially attributed to methodological differences in crater size measurement and imagery dataset used for crater mapping, the identification and removal of areas contaminated by secondary craters as well as the variability in the identification and inclusion of degraded and/or buried impact structures. Area #21 (50.06 km^2) from Giguere et al. (2022) is limited to the immediate vicinity of the Chang'e-5 landing site and is fully included in other larger areas investigated in other studies (Jia et al., 2020; Qian et al., 2018, 2021; Morota et al., 2011). For example, Qian et al. (2018) counted 14 craters >200 m on this area using Kaguya Terrain Camera (TC) images whereas Giguere et al. (2022) reported 46 craters >200 m using LROC NAC images with multiples incidence angles, leading to significant variation in derived $N(1)$ values.

Here, we perform a crater density measurement over Area #21 using a convolutional neural network-based Crater Detection Algorithm (Benedix et al., 2020; Lagain et al., 2021a, 2021b; Fairweather et al., 2022, 2023), specifically trained on Kaguya TC images (Haruyama et al., 2008). Craters detected over the counting area are shown in Fig. 4a, and those >100 m in diameter (607 in total) are used in the $N(1)$ measurement (Fig. 4c). Although the size of craters detected by our algorithm substantially differ from those measured by Giguere et al. (2022) or Qian et al. (2018) (Fig. 4b), the derived $N(1)$ value inferred from the detections using the CraterStatsII software (Michael and Neukum, 2010) and the lunar chronology system from Neukum et al. (2001) sits at 2.67 × 10^{-3} km^{-2} (Fig. 4c). This crater density value is very similar to that reported by Giguere et al. (2022) (2.61 × 10^{-3} km^{-2}) obtained from the counting of 181 craters ranging between 100 m and 600 m (of which 83 between 180 m and 600 m were used in the $N(1)$ derivation) on Area #21. The difference in crater densities between all these measurements is most likely due to the inclusion of buried craters by thin lava flows. Morphological characteristics allowing to distinguish buried craters from the superposed and degraded ones are extremely subtle and subject to interpretation whatever the methods (automatic or manual) and the data (imagery or topography) used to identify them. Despite the variety of published crater densities measured around the landing site, and in the absence of a consensus about the most accurate and the most representative crater count associated to this sample, we use the $N(1)$ value from Giguere et al. (2022), consistent with the crater density we infer from our automatic approach, to recalibrate the chronology (see next section).

3. Results

3.1. The lunar crater chronology recalibration

$N(1)$ is an extrapolation of the crater density directly measured for craters larger than a given size D (Table 1). Those reported in the literature are derived from two different production functions (PFs), namely Neukum et al. (2001) and Neukum (1983). Both PFs are

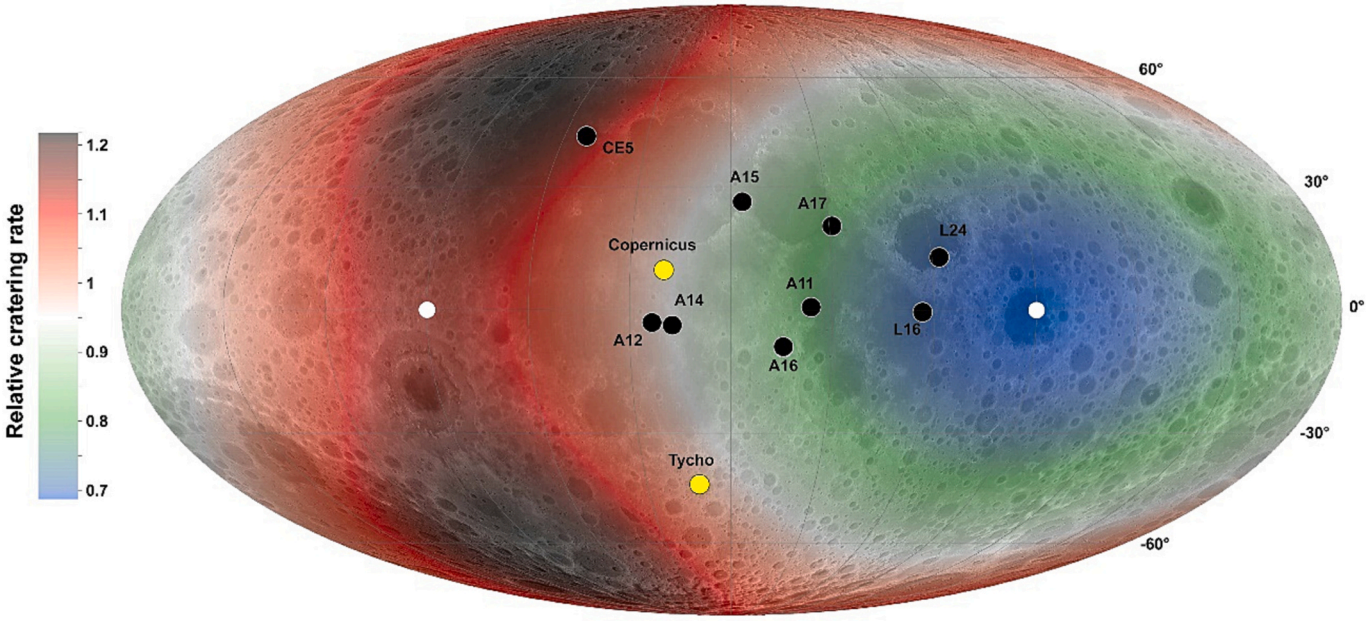

Fig. 3. The asymmetry of the lunar cratering rate. The combination of impact flux models (Gallant et al., 2009; Robertson et al., 2021, 2023), the impact-velocity (Wang and Zhou, 2016) and the impact-angle variabilities (Robertson et al., 2021, 2023) are used to compute the relative cratering rate (available in Dataset S1). The location of lunar samples collected and used in the calibration of the chronology are also shown, and Tycho and Copernicus craters are marked in yellow as these sites are indirect constraints of the lunar cratering rate (Stöffler and Ryder, 2001). The apex and antapex of motion are marked by white dots. Background: LRO-WAC mosaic. A: Apollo, L: Luna, CE: Chang'e. Interval grid: 30°. (For interpretation of the references to colour in this figure legend, the reader is referred to the web version of this article.)

polynomial fit to the cumulative number of lunar craters N per surface area per billion years, with diameters larger than D (valid for D in the range 10 m–300 km) and have similar relationships with different coefficients given in Table 2. They can be expressed as:

$$log_{10}(N) = a_0 + \sum_{n=1}^{11} a_n [log_{10}(D)]^n, \quad (14)$$

Homogenization of the PF used to infer $N(1)$ is required prior to the recalibration of the lunar cratering chronology. Here, we convert all $N(1)$ crater densities measured from the PF of Neukum (1983) to the crater density obtained from the PF of Neukum et al. (2001), noted $N(1)^*$:

$$N(1)^* = N(1) \times 10^{\sum_{n=1}^{11} [(a_n^* - a_n) log_{10} D]^n}, \quad (15)$$

where a_n and a_n^* are the coefficients from Neukum (1983) and Neukum et al. (2001), respectively (Table 2), and D is the minimum crater diameter used to derive $N(1)$ (Table 1). We note that the difference between $N(1)^*$ and $N(1)$ is moderate and varies from −0.8% to 12.1%. The crater density $N(1)^*$ thus obtained is then corrected from the spatial variation of the cratering rate, as described in Eq.13. Results are given for $\lambda = 0°$ and $\varphi = 0°$ (i.e., at the equator and the meridian) in Table 1. $N(1)^*$ corrected from any spatial variation of the cratering rate is then used to recalibrate the lunar cratering chronology (Fig. 5).

The chronology function of Neukum et al. (2001) is expressed as the sum of an exponential and linear component: $N(1) = \alpha(e^{\beta T} - 1) + \gamma T$, where α, β, and γ coefficients are equal to 5.44×10^{-14}, 6.93, and 8.38×10^{-4} in the Neukum's chronology model, and T is the age of the surface in Ga (Fig. 5). We fitted the spatially corrected crater densities and radiometric ages of lunar samples using a similar function and the Trust-Region Algorithm of the non-linear least-square fitting to solve α, β, and γ coefficients. The sum of squared residuals was minimized through iteration, and coefficients from Neukum et al. (2001) were used as the initial values. R^2 stabilized at 0.97, the adjusted-R^2 at 0.97, and the SSE (summed square of residuals) at 5.22×10^{-5}, for α, β, and γ equal to 1.52×10^{-14}, 7.38, and 9.52×10^{-4}, respectively.

The function, valid at 0°N, 0°W, needs to be adapted to other locations on the Moon's surface (Fig. 3) and is shown in Fig. 5 (red curve), along with its variability depending on the location of the considered area on the globe (grey area). It is expressed as follows for 0°N, 0°W: $N(1) = 1.52 \times 10^{-14}(e^{7.38 \times T} - 1) + 9.52 \times 10^{-4} T$, where T is the model age in billion years.

A comparison of our chronology with other models proposed over the last two decades (Neukum et al., 2001; Hartmann et al., 2007; Marchi et al., 2009; Le Feuvre and Wieczorek, 2011; Robbins, 2014) is also shown in Figs. A.1 and A.2, and coefficients of other functions are available in Table 3. We note that corrected for spatial variation in the cratering rate, lower $N(1)$ values previously reported for the Chang'e-5 landing site (1.74×10^{-3} km^{-2}, Jia et al. (2020); 1.24×10^{-3} km^{-2}, Williams et al. (2018); 1.28×10^{-3} km^{-2}, Qian et al. (2021)) give 1.51×10^{-3} km^{-2}, 1.08×10^{-3} km^{-2}, 1.11×10^{-3} km^{-2}, respectively. When corrected, our $N(1)$ value measured from automatic crater detections gives 2.27×10^{-3} km^{-2}. If these corrected crater densities are used in the recalibration of the chronology function, the quality of the resulting fits are not statistically different from the one obtained using Giguere's measurement. The coefficients α, β, and γ of the lunar chronology function as well as the R^2, adjusted-R^2 and SSE values associated with each fit are given in Table 3.

3.2. Implications for the lunar chronology

Except Chang'e-5, all calibration points used to constrain the lunar chronology are located very close to the equator, and only two samples were collected in areas above 20° in latitude: namely Apollo 15 and Apollo 17 (Fig. 3, Table 1). Based on our results, the association of these sample ages and the measured crater density of their source terrains is only representative of the lowest crater accumulation rate on the Moon. Conversely, the Chang'e-5 mission landing site is the closest to the region where the cratering rate is found to be the highest and is representative

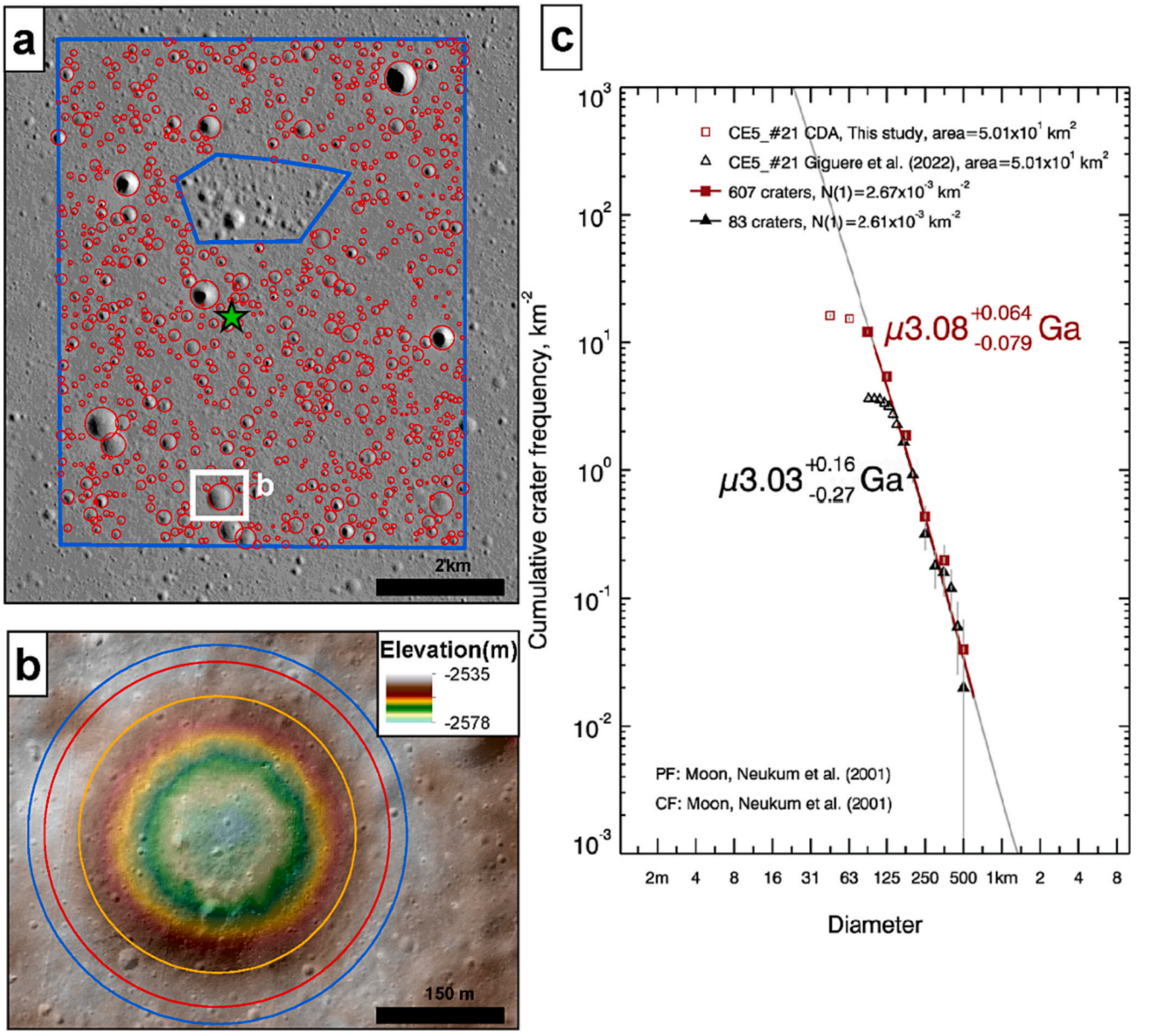

Fig. 4. Automatic crater counts and crater density measurement around the Chang'e-5 landing site (Area #21 from Giguere et al. (2022)). a: Detections over the Kaguya TC global mosaic (Haruyama et al., 2008). The counting area is shown in blue and is the same as in Giguere's study. The green star denotes the landing site and the white square shows the location of the crater shown in panel b. b: Close-up showing the crater #6 discussed by Giguere et al. (their fig. 7) over the LRO-NAC mosaic and the LRO-NAC DTM of the Chang'e-5 landing site, both available at https://wms.lroc.asu.edu/. The diameter of this crater, as identified by our algorithm, is 407 m (red circle). The orange and blue circles correspond to the crater size as measured by Qian et al. (2018) (327 m) and Giguere et al. (2022) (446 m), respectively. c: The fit of the Size-Frequency Distribution of craters detected by our algorithm (in red) between 100 m and 600 m in size gives a $N(1)$ value of 2.67×10^{-3} km^2. The CSFD measured by Giguere et al. is shown in black and gives a similar $N(1)$ value using craters ranging from 180 m to 600 m in diameter: 2.61×10^{-3} km^2. (For interpretation of the references to colour in this figure legend, the reader is referred to the web version of this article.)

of a cratering rate about 28% higher than at the equator and the meridian. Although the addition of the corrected new calibration point from Chang'e-5 samples does not significantly change model ages compared to a previous chronology model (Neukum et al., 2001) under the assumption of isotropic impact flux, angle, and speed (Fig. 5), the variability of these parameters across the lunar surface significantly changes model ages between ~3.4 Ga and ~0.5 Ga inferred from crater counts. Therefore, this applies to Eratosthenian and Copernican impact craters, as well as terrains resulting from a late volcanic activity such as the Mons Rümker and Eratosthenian terrains in Oceanus Procellarum and Mare Insularum (Hiesinger et al., 2003; Morota et al., 2011; Richardson and Abramov, 2020).

Using our new chronology model, a surface located at 90°W, 60°N previously interpreted as having a 3 Ga model age using Neukum's chronology is more likely to be ~0.8 Ga younger, so ~2.2 Ga old. Conversely, equatorial regions close to the antapex of motion would be older by ~600 Ma in a case where a 2.5 Ga old model age is derived from the Neukum's chronology system. We note that the influence of the spatial variation of the cratering-rate prior to 3.5 Ga can be considered as negligible in the model age derivation (Fig. 6a). In other words, hypothetical spatial variation of the cratering rate in ancient time (>3.5 Ga) would not significantly affect model ages inferred for old units, unless this variability was an order of magnitude higher than currently reported. Because Le Feuvre and Wieczorek (2011) determined a higher impact flux at the equator than at the poles, the difference in model ages between their system and ours with respect to the latitudes is higher:

Table 1
Calibration points used in the recalibration of the lunar cratering curve. $N(1)$ is the value reported in the literature ([a]Norman, 2009; [b]Stöffler and Ryder, 2001; [c]Giguere et al., 2022; [d]Hiesinger et al., 2012), and $N(1)^*$ is equivalent to $N(1)$ when derived from the PF of Neukum et al. (2001). The last column corresponds to $N(1)^*$ corrected from spatial variations of the cratering rate, valid at the equator and the meridian. The minimum crater diameter used to infer the $N(1)$ value using the Neukum (1983) PF is also mentioned.

Site	Latitude (°)	Longitude (°)	Age (Ga)	$N(1)$ (km^{-2})	D used in $N(1)$ derivation	$N(1)^*$ (km^{-2})	$N(1)^*$ corrected (km^{-2})
Descartes Formation (A16)[a]	−8.97	15.50	3.866 ± 0.009	$3.47 \times 10^{-2} \pm 7.00 \times 10^{-3}$	0.4 km	3.47×10^{-2}	4.12×10^{-2}
Fra Mauro Formation (A14)[b]	−3.64	−17.47	3.85 ± 0.02	$3.70 \times 10^{-2} \pm 7.00 \times 10^{-3}$	2 km	4.21×10^{-2}	4.34×10^{-2}
Mare Serenitatis (A17)[b]	20.19	30.77	3.75 ± 0.01	$1.00 \times 10^{-2} \pm 3.00 \times 10^{-3}$	0.4 km	1.01×10^{-2}	1.26×10^{-2}
Mare Tranquilitatis (A11)[b]	0.67	23.47	3.60 ± 0.01	$6.42 \times 10^{-3} \pm 5.40 \times 10^{-4}$		6.42×10^{-3}	7.91×10^{-3}
Mare Imbrium (A15)[b]	26.13	3.50	3.30 ± 0.02	$3.20 \times 10^{-3} \pm 1.10 \times 10^{-3}$	2 km	3.64×10^{-3}	3.97×10^{-3}
Oceanus Procellarum (A12)[b]	−3.01	−23.42	3.15 ± 0.04	$2.81 \times 10^{-3} \pm 9.93 \times 10^{-4}$		2.81×10^{-3}	2.83×10^{-3}
Mare Fecunditatis (L16)[b]	−0.51	56.37	3.41 ± 0.04	$3.30 \times 10^{-3} \pm 1.00 \times 10^{-3}$	0.7 km	3.27×10^{-3}	4.54×10^{-3}
Mare Crisium(L24)[b]	12.71	62.20	3.22 ± 0.02	$3.00 \times 10^{-2} \pm 6.00 \times 10^{-4}$	0.9 km	2.98×10^{-3}	4.14×10^{-3}
Northern Oceanus Procellarum (CE5)[c]	43.05	−51.80	2.03 ± 0.004	$2.61 \times 10^{-3} \pm 8.10 \times 10^{-5}$		2.61×10^{-3}	2.27×10^{-3}
Copernicus (indirect measurement)[d]	9.62	−20.08	0.78 ± 0.015	$6.67 \times 10^{-4} \pm 5.27 \times 10^{-5}$		6.67×10^{-4}	6.77×10^{-4}
Tycho (indirect measurement)[d]	−43.31	−11.36	0.109 ± 0.004	$7.12 \times 10^{-5} \pm 1.88 \times 10^{-5}$		7.12×10^{-5}	6.88×10^{-5}
North Ray (A16)[d]	−8.82	15.48	0.053 ± 0.008	$3.84 \times 10^{-5} \pm 1.14 \times 10^{-5}$		3.84×10^{-5}	4.55×10^{-5}
Cone (A14)[b]	−3.62	−17.43	0.025 ± 0.012	$2.10 \times 10^{-5} \pm 5.00 \times 10^{-6}$	0.03 km	2.16×10^{-5}	2.23×10^{-5}

Table 2
Coefficients of the PFs (Neukum, 1983; Neukum et al., 2001) used in Eq.15.

a_i	Neukum (1983)	Neukum et al. (2001)
a_1	−3.6269	−3.557528
a_2	0.4366	0.781027
a_3	0.7935	1.021521
a_4	0.0865	−0.156012
a_5	−0.2649	−0.444058
a_6	−0.0664	0.019977
a_7	0.0379	0.086850
a_8	0.0106	−0.005874
a_9	−0.0022	−0.006809
a_{10}	−0.000518	0.000825
a_{11}	0.0000397	0.0000554

considering three ~3.5 Ga old surfaces according to Le Feuvre and Wieczorek's chronology, all located at the apex but at different latitudes (±60°N, ±30°N, and equator), the resulting model ages using our model would be ~2.5 Ga, ~3.0 Ga, and ~ 3.2 Ga, respectively (Fig. 6b). The difference in model ages derived from our model and that of Le Feuvre and Wieczorek (2011) becomes negligeable beyond ~3.7 Ga.

In rare cases, the dependency of terrain location in the accumulated number of craters over time might thus lead to a younger surface, exhibiting more craters and located close to the poles and the apex of motion, compared to another one close to the equator and the antapex. Accounting for model ages of craters >50 km in diameter (Kirchoff et al., 2021), we found that this situation occurs for Kirkwood (68°N, 157°W, D = 68 km, N(1) = 3.2×10^{-3} km^2) and Plutarch (24°N, 79°E, D = 70 km, N(1) = 2.7×10^{-3} km^2) craters. Model ages inferred for these two craters are 2.4 ± 0.3 Ga and 2.1 ± 0.4 Ga in Marchi's chronology (Marchi et al., 2009), respectively (3.3 Ga and 3.1 Ga using Neukum's chronology), while we obtain 2.9 Ga and 3.3 Ga using our spatial variable chronology system. Although the relative chronology of these two impact events is inverted when model ages are derived from spatial dependent chronology, the difference in model ages is within the uncertainty of the crater counting method.

This new chronology has consequences when it comes to analyzing the model-age distribution of impact craters and relates its potential variation to the orbital dynamics of impactor reservoirs. Applying our chronology to a set of crater ages (Kirchoff et al., 2021) leads to a relatively constant formation rate of craters >50 km formed over the last ~3 Ga as well as to the disappearance of sharp increases of crater formation obtained at ~2.1 Ga, ~3.1 Ga, and ~ 2 Ga using Marchi's, Neukum's and Le Feuvre and Wieczorek's chronology models, respectively (Fig. 7 and Appendix B). Although temporal variations could be tested through the analysis of a larger set of crater ages, this observation is in line with the commonly accepted constant impact flux for this diameter range (e.g., Neukum et al., 2001; Lagain et al., 2022 and references therein) and potentially challenges the existence of a significant decoupling of the cratering rate between large and small craters postulated in earlier works (e.g., Mazrouei et al., 2019; Lagain et al., 2020). Nevertheless, a lull and an increase in the formation of asteroid families near resonances that efficiently deliver large asteroids (diameter > 3.5 km) to encounter orbits with the Earth-Moon system, and thus overcoming the background cratering rate (Bottke et al., 2007, 2015), might theoretically cause such decoupling. The absence of such signal using our chronology could also suggest that the crater size range considered in Kirchoff et al. (2021) is not affected by such flux variations following potential break-up events. This could be tested through the analysis of model ages of smaller craters.

4. Discussion

4.1. The influence of the Earth-Moon distance variation

Considering that the Moon is assumed to be tidally locked for the past 4 Ga (Ćuk et al., 2016), and that the Earth-Moon distance considerably increased through time, we assess the influence of this parameter in the change of the orbital speed of our satellite as well as the gravitational focusing effect, and thus in the relative cratering rate with respect to the

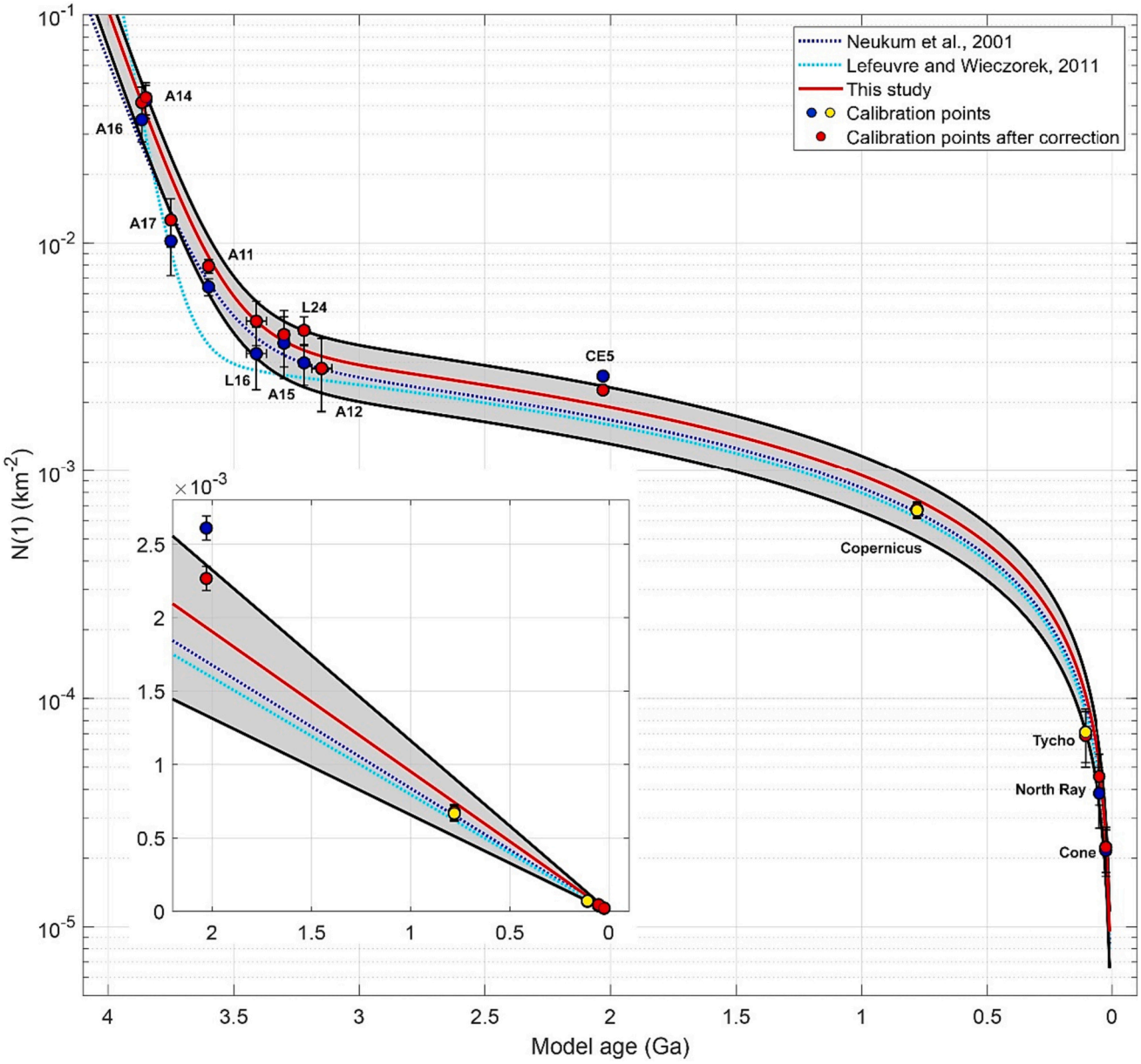

Fig. 5. The spatial-dependent lunar cratering chronology. Calibration points listed in Table 1 are shown before (blue and yellow dots) and after (red dots) correction accounting for the spatial variability of the cratering rate, normalized at 0°N, 0°E. Yellow dots denote indirect constraints of the lunar cratering rate (Stöffler and Ryder, 2001). The red curve is the chronology model obtained after data correction. The grey area shows the variability of our chronology model depending on the location on the lunar surface (high latitudes/apex (±60°N, 90°W): upper black curve; equator/antapex (0°N, 90°E): lower black curve). Neukum's and Le Feuvre and Wieczorek's chronologies (valid at 0°N, 0°E) are also given for comparison. (For interpretation of the references to colour in this figure legend, the reader is referred to the web version of this article.)

distance of the apex of motion computed using Eq.13. Accounting for the Earth-Moon distance evolution (Farhat et al., 2022) (Fig. 8a) and assuming a lunar circular orbit over its entire history, we infer that the mean orbital velocity of the Moon 4 Ga ago (at 35 E_r (Earth radii)) was 1.34 km/s (Fig. 8b), and that the apex/antapex cratering asymmetry is only enhanced by ~2.5% compared to the present period (Fig. 8c). Because it is assumed that the Moon has spent the last 3.5 Ga beyond 40 E_r (Farhat et al., 2022), we choose to consider the effect of the varying Earth-Moon distance with time negligible.

To determine the effect of gravitational focusing on the lunar impact rate over time, we assume a constant source population over geological time, thus isolating the effect purely due to focusing from the Earth. The debiased NEO orbital distribution (Granvik et al., 2018) is the source population, and the encounter radiant distribution is determined using previously published methodology (Pokorný and Vokrouhlický, 2013). From this radiant distribution, a simulation of 190 million fictitious encounters is used to reconstruct the gravitational focusing in the Earth-Moon system at a given Earth-Moon distance (Farhat et al., 2022). A symplectic Wisdom-Holman integrator implemented in Python by the Rebound N-body integration package is utilized to integrate the particles in this simulation (Rein and Liu, 2012; Rein and Tamayo, 2015). The lunar impact flux is then determined by the relative flux found near the Moon's estimated position at each moment given by the tidal model (Fig. 8d). We find that the impact flux 4 Ga ago was only enhanced by ~2% compared to present time due to the closer Earth-Moon distance. Therefore, both the variation in time of the gravitational focusing of the Earth and encounter velocity are of very moderate effects, confirming earlier results (Le Feuvre and Wieczorek, 2011), and are considered

Table 3
Coefficients of chronology functions shown in Appendix A. Coefficients for the model presented in this study and from Le Feuvre and Wieczorek (2011) are valid at the equator and the meridian. Note that chronologies proposed by Robbins (2014) and Hartmann et al. (2007) include a quadratic term that reflects a linear decrease in the crater accumulation over the last ~2 Ga and ~ 3.5 Ga respectively: $N(1) = \alpha(e^{\beta T} - 1) + \gamma T^2 + \delta T$. In any case, the last coefficient represents the current impact cratering rate for craters >1 km in diameter. The different $N(1)$ values used in this study are from [a]Giguere et al. (2022), [b]Jia et al. (2020), [c]Wu et al. (2018), [d]Qian et al. (2021), and our automatic crater count[e], after being corrected from the spatial variability of the cratering rate.

Chronology model	R^2	Adjusted-R^2	SSE	α	β	γ	Δ
Neukum et al. (2001)	–	–	–	5.44×10^{-14}	6.93	8.38×10^{-4}	–
Hartmann et al. (2007)	–	–	–	4.45×10^{-11}	5.17	1.14×10^{-4}	2.82×10^{-4}
Marchi et al. (2009)	–	–	–	1.23×10^{-15}	7.85	1.30×10^{-3}	–
Le Feuvre and Wieczorek (2011)	–	–	–	1.89×10^{-15}	14.44	7.96×10^{-4}	–
Robbins (2014)	–	–	–	7.26×10^{-41}	22.6	1.88×10^{-4}	9.49×10^{-4}
This study[a]	0.99	0.99	3.41×10^{-5}	1.52×10^{-14}	7.38	9.52×10^{-4}	–
This study[b]	0.99	0.99	3.18×10^{-5}	1.67×10^{-14}	7.62	8.56×10^{-4}	–
This study[c]	0.99	0.99	3.39×10^{-5}	1.63×10^{-14}	7.37	8.62×10^{-4}	–
This study[d]	0.97	0.96	9.17×10^{-5}	9.31×10^{-14}	6.93	5.80×10^{-4}	–
This study[e]	0.99	0.99	3.41×10^{-5}	1.52×10^{-14}	7.38	9.52×10^{-4}	

negligeable in this study.

4.2. The temporal limit of the cratering rate spatial variation

The spatial cratering rate variability we discuss in this work is obtained from collisional probabilities of the current population of impactors, namely NEOs. Nevertheless, the early instability of giant planets is thought to have led to a change in the impactor population from leftovers to asteroids ~3.5 Ga ago (Bottke et al., 2015; Morbidelli et al., 2018; Xie et al., 2021; Nesvorný et al., 2017, 2022). The spatial anisotropy of the lunar bombardment could therefore be questioned on a geological timescale.

Previous works studied the spatial distribution of fresh craters on the lunar surface (e.g., Kreslavsky et al., 2012; Werner and Medvedev, 2010; Morota and Furumoto, 2003; Williams et al., 2018) The leading/trailing asymmetry of the cratering rate has been investigated through the distribution of 43 m–2.3 km cold spots in a ± 45° latitude band, namely low night-time temperature anomalies associated with impacts formed no later than 100 ka–1 Ma ago (Williams et al., 2018), as well as through the population of 222 rayed craters >5 km in diameter and located at low latitudes on lunar highlands (Morota and Furumoto, 2003). The lifetime of rays surrounding impact craters on the Moon is estimated to be about 750 Ma–1 Ga (Morota and Furumoto, 2003; Werner and Medvedev, 2010). In addition, latitudinal heterogeneities of the cratering rate were previously explored through the population of 1615 rayed craters as small as 1 km in diameter identified between latitudes ±70° (Werner and Medvedev, 2010). This population, corrected from the influence of Mare units in their detectability (Werner and Medvedev, 2010), will be used to test the latitudinal asymmetry of the cratering rate asymmetry over the last ~1 Ga.

In order to push back the temporal limit of the comparison between the spatial distribution of recent craters formed on the Moon and that of NEO impact probabilities, we analyze the distribution of lunar craters with size ranging between 3 and 10 km (impactor diameter between ~150 m and ~550 m) from the lunar crater database (Robbins, 2019), accumulated on pre-Nectarian and Nectarian terrains (115,587 craters), independently (Fig. 9, Table 4). We used the global geological map of the Moon (Fortezzo et al., 2020) to exclude secondary crater chains and areas associated with Mare, and more generally Copernican, Eratosthenian and Imbrian areas due to their younger ages compared to the surrounding highlands provinces and the wide formation age these units exhibit. Although geological mapping and unit's age are, in some cases, fully dependent on crater statistics, potential spatial variations of the cratering rate lead to minimal differences in crater density between old terrains (Pre-Nectarian and Nectarian) and younger units (Fig. 9). Therefore, we consider negligeable the contribution of the spatial variation of the cratering rate in the mapping of old units epoch formation. We excluded areas associated with Mare Orientale due to large-scale crater obliteration induced by this impact and its ejecta on the nearside. The geographic distribution of pre-nectarian and nectarian terrains selected here does not allow to analyze with confidence the spatial distribution of large lunar craters with respect to their distance with the apex of motion. Indeed, terrains close to the apex are dominated by materials associated with Mare Orientale. For this reason, only the latitudinal distribution of large craters superposed on old terrains is analyzed in this study.

While the 3–10 km crater population on pre-Nectarian and Nectarian units was mostly formed 3.5–4 Ga ago by planetary leftovers and comet populations (Bottke et al., 2015; Morbidelli et al., 2018; Xie et al., 2021; Nesvorný et al., 2017, 2022), the analysis of their spatial distribution relies on several critical assumptions that are further discussed in Appendix C: (1) the accumulation and retention of craters on the surface needs to average out and potential spatial variation of crater erasure processes has to not be efficient enough to counteract the signal of a spatial-varying flux, (2) the secondary-crater contamination is negligible or homogeneous across considered surfaces, (3) the crater population did not reach a saturation equilibrium, (4) the amplitude of potential True Polar Wander (TPW) events and/or obliquity variations were limited enough to not compensate for hypothetical geographical variation of the cratering rate.

Three sets of crater density measurements were performed with the same number of craters within each size range on pre-Nectarian (41,583 craters in total) and Nectarian terrains (74,004 craters in total) to ensure enough craters are contained in each bin. The crater density is computed using the lunar ellipsoid over 20° bin from the equator over selected geological units (Fig. 9). The area A used in each bin is set as the intersection between the quadrangle defined by the edge of each latitudinal band and the total area presented in Fig. 9. The relative cratering density for each bin is defined as $\frac{\eta(D)/A}{\eta_T/A_T}$, where $\eta(D)$ is the number of craters within a given size range contained in each collecting surface of an area A, η_T is the total number of impact craters within the same diameter range contained in the entire surface A_T. Errors are defined as $\frac{\sqrt{\eta(D)}/A}{\eta_T/A_T}$. Results of the relative crater density with respect to the latitude are presented in Appendix D.

Fig. 10 shows the cratering rate with respect to the distance from the equator inferred from the impact flux and angle distribution (Robertson et al., 2021, 2023) (panels a and b), as well as the relative cratering rate obtained from the impact flux and impact velocity distribution with respect to the distance from the apex (Gallant et al., 2009; Wang and Zhou, 2016) (panel c). The rayed craters population identified by

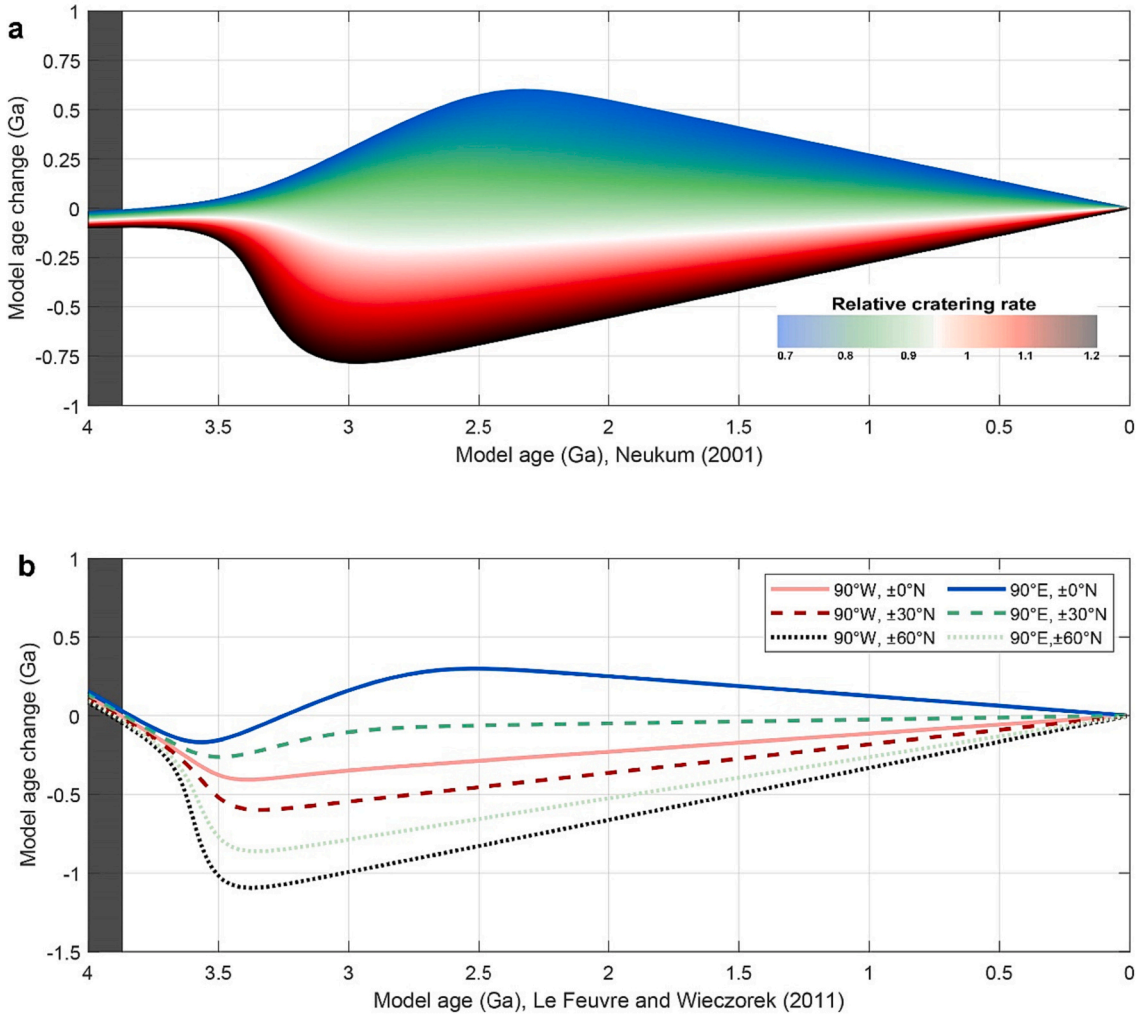

Fig. 6. Influence of the variability of the cratering rate on lunar chronology models. a: Model age difference between the new chronology model presented in this study and that of Neukum et al. (2001), with respect to Neukum's model age and the relative cratering rate. As an example, a model age of 2 Ga inferred from the Neukum's chronology for a terrain located at 90°E, 0°N would be ~500 Ma older using our chronology system. The grey area indicates the time range for which the chronology is not constrained (> 3.9 Ga) due to a lack of calibration points. The colors match with the relative cratering rate shown in Fig. 3. b: Same as panel (a), with respect to Le Feuvre and Wieczorek (2011) model age at different locations on the Moon. For example, a surface located at the antapex and the equator with an age of ~2.5 Ga inferred with Le Feuvre and Wieczorek's chronology would be ~300 Ma older using our chronology.

Werner and Medvedev (2010), corrected for the more rapid-fading in mare areas (in grey in Fig. 10a and b), exhibits a pole/equator density ratio of ~1.32, higher than the ~1.26 ratio inferred from our model. The spatial distribution of cold spots (Williams et al., 2018) reveals an apex/antapex ratio of ~1.95 (in green in Fig. 10c) while the rayed crater population (Morota and Furumoto, 2003) leads to a ratio of 1.52 (in blue in Fig. 10c). The apex/antapex ratio from our cratering rate model sits in between, at ~1.68.

The 3–10 km craters distribution shows a relative crater density increase with the distance from the equator (Fig. 10a and b). The differences between the measured crater density and a uniform crater distribution are significant, supported by very narrow error bars. The amplitude of the crater-density increase with latitude is in general more pronounced than the relative cratering-rate prediction for both terrain types (red stars on Fig. 10a and b). The pole/equator crater density ratio on pre-Nectarian and Nectarian units is on average 1.22 and 1.32 (when smoothed over latitudes 0°–30° and 60°–90° from the equator), respectively. It is also worth noting that the high concentration of small craters (<5 km in diameter) located close to the north pole relative to the equator (Figs. 10a, b and D.1) was also reported in a previous work (Robbins, 2019) and that the NEO impact statistics available at that time (Bottke et al., 2002) were not able to explain this result (Robbins, 2019). We also found that the relative density of craters for the two first size ranges are similar and follow a relatively symmetric distribution, centered around the equator, which is less pronounced for craters >4.87 km (Fig. D1). Likewise, the relative crater density for D > 4.87 km beyond 60° from the equator on both terrain types is significantly different from the two smaller diameter ranges. The small surface considered at these latitudes (Tables D.1 and D.2) or a difference in the accumulation and retention rate of larger craters close to the poles compared to the smaller ones might be responsible for this difference. For example, the cookie-cutting process being scale-dependent (Riedel et al., 2020, Appendix C), a higher impact flux at the poles could lead to a higher erasure rate of large craters than the small ones. Similarly, a higher impact flux of small impactors at the equator due to the gravitational focusing of the Earth would cause a higher erasure rate of larger craters than at the poles. However, this effect will not counterbalance the increasing flux with the latitudes and cannot explain the observed crater distribution for different size ranges. The distribution of rayed craters (Werner and Medvedev, 2010) produces, however, a much higher relative crater density compared to our observations, in particular between 50° and 70° from the equator.

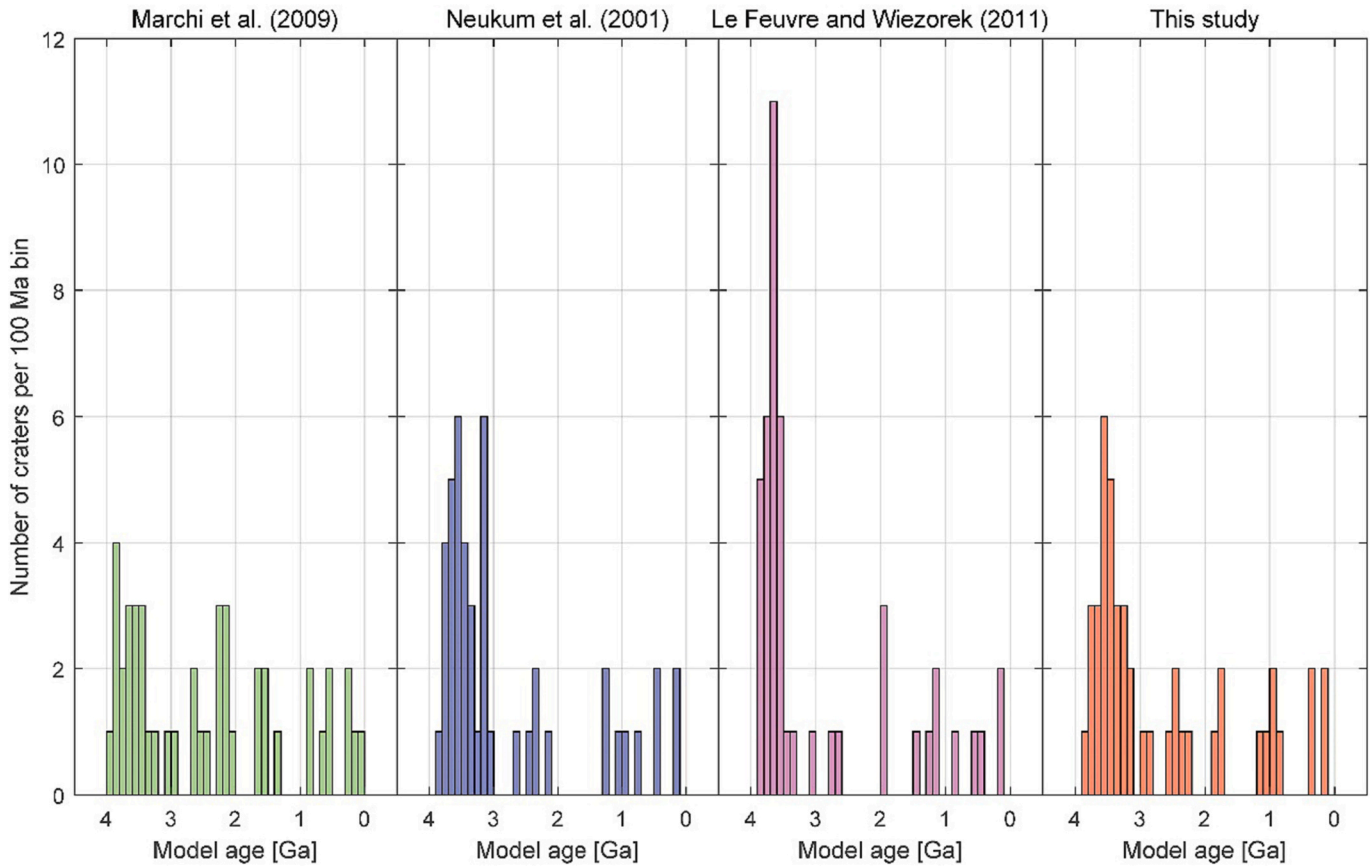

Fig. 7. Comparison of model age distribution of craters > 50 km in diameter reported by Kirchoff et al. (2021). In green, using the chronology system proposed by Marchi et al. (2009) (modified from Kirchoff et al., 2021), in blue, using Neukum's chronology, in pink, using Le Feuvre and Wieczorek's chronology, and in red with our spatial dependent chronology system. (For interpretation of the references to colour in this figure legend, the reader is referred to the web version of this article.)

Although the amplitude of the crater distribution on pre-Nectarian and Nectarian terrains (resulting from the retention of craters formed over the last ~4 Ga) differs greatly from that of the cratering rate predictions, it follows the general increase with the distance from the equator. Our model compares well (in trend and amplitude) with the distribution of rayed craters from Morota and Furumoto (2003). These observations suggest the possibility that the spatial dependency of the impact flux and approach conditions of impactors having formed the cold spots, rayed craters and older craters analyzed here presented orbital distributions that somehow mimic the current NEO population, i.e., presenting an excess of high-inclined encounters, and that the synchronicity of the lunar orbit influenced the cratering distribution on a geological timescale. Thus, the trend of the spatial distribution of craters superposed on the highlands could suggest that: (1) the orbital characteristics of ancient impactors prior to ~3.5 Ga was potentially heterogeneous and led to an excess of impacts in polar regions, and (2) the distribution of the current NEO population orbital characteristics could have been inherited from those of ancient impactor populations.

Because the crater distributions are influenced by geological processes of various origins (see Appendix C), the spatial variations of the crater density measured here and reported in earlier studies cannot be used to precisely quantify the heterogeneity of the cratering rate over geological timescale. Nonetheless, we do not exclude the possibility that the spatial dependency of the cratering rate caused by NEO population constitutes a minimum over long periods of time, considering that they are lower than the relative cratering rate inferred from the various cratering distributions. Likewise, it is most likely that the amplitude of the variations in the impact flux and impact angles with respect to the latitudes changed over time as a result of the formation and dissipation of new asteroid families. The general increase of the cratering density observed with the latitudes for the different crater populations presented here is however consistent with the recent model of NEOs impact probability (Robertson et al., 2021, 2023).

5. Conclusion

We computed the spatial variation of the cratering rate on the Moon using updated latitudinal dependencies of the impact flux and angles as well as the variation of the flux and speed of encounters with respect to the distance from the lunar apex. Our model compares relatively well with the previously unexplained spatial density increase with the latitudes of rayed craters formed over the last ~1 Ga on the Moon. The trend of the latitudinal distribution of craters on pre-Nectarian and Nectarian units suggests that the lunar cratering rate spatial variation might be similar (in trend, not in amplitude) for periods prior to ~3.5 Ga. The latitudinal dependency, as opposed to that previously reported (Le Feuvre and Wieczorek, 2008, 2011), is most likely due to an excess of asteroids with highly-inclined orbits (Robertson et al., 2021).

Corrected for the spatial variation of the cratering rate, calibration points used to constrain the lunar chronology model allow to derive a new spatially dependent chronology function. The correction applied to the crater count performed by Giguere et al. (2022) around the Chang'e-5 landing site and through automatic detection (this work) allows to reconcile the exceptionally high crater density with the age of the samples (Giguere et al., 2022; Li et al., 2021). Our results lead to substantial changes in model ages derived from crater counts on terrains younger than ~3.5 Ga old with respect to Neukum et al. (2001) and Le Feuvre and Wieczorek (2011) chronologies: differences up to ~30% in model ages could be observed. The sequence of lunar impact events inferred by a previous study (Kirchoff et al., 2021) is thus significantly

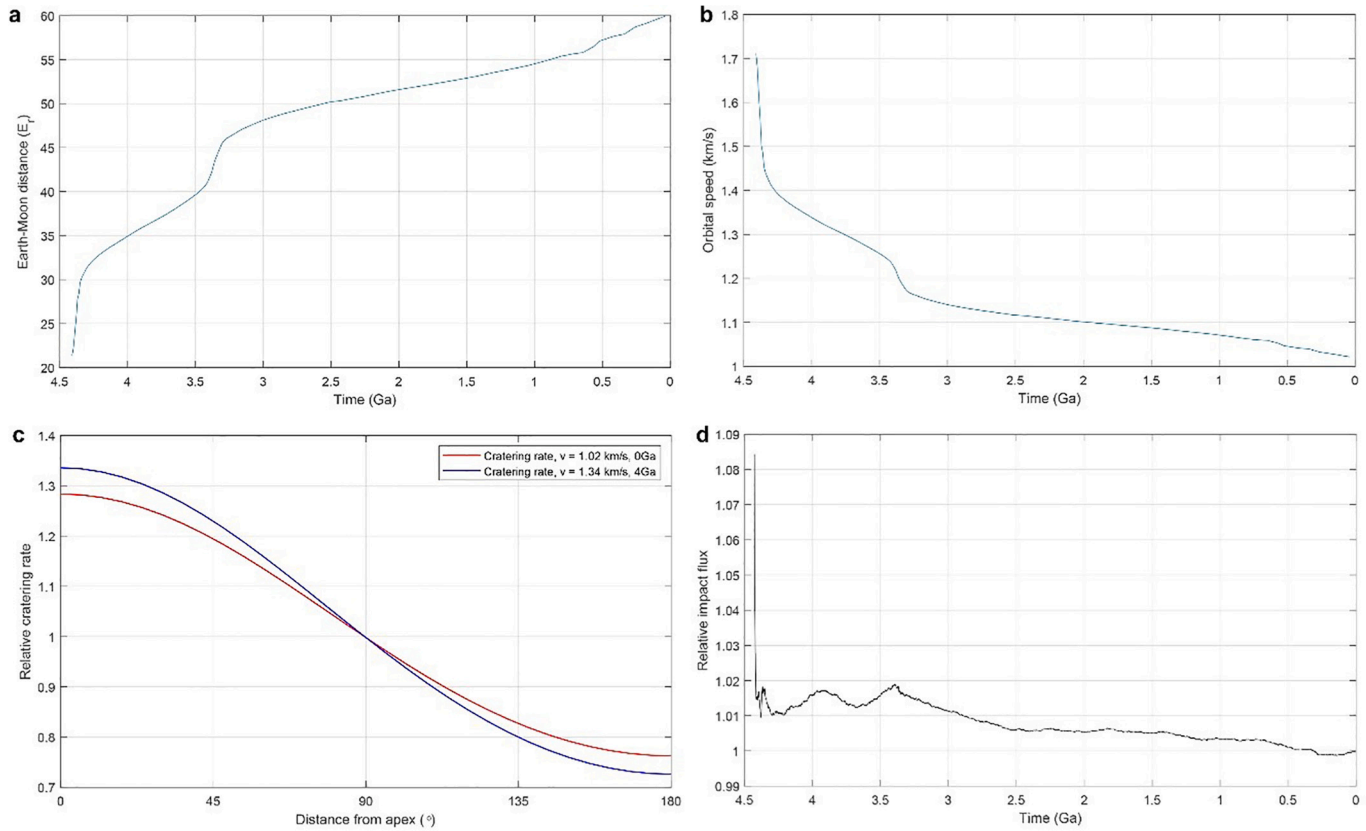

Fig. 8. Effect of the Earth-Moon distance in the relative cratering rate. a: Evolution of the Earth-Moon distance (in Earth radii, E_r) through time (Farhat et al., 2022). b: Temporal evolution of the orbital velocity of the Moon. c: Relative crater density with respect to the distance from the apex at 35 E_r (4 Ga ago, in blue) and 60 E_r (present time, in red). d: Variation of the lunar impact flux due to gravitational focusing. (For interpretation of the references to colour in this figure legend, the reader is referred to the web version of this article.)

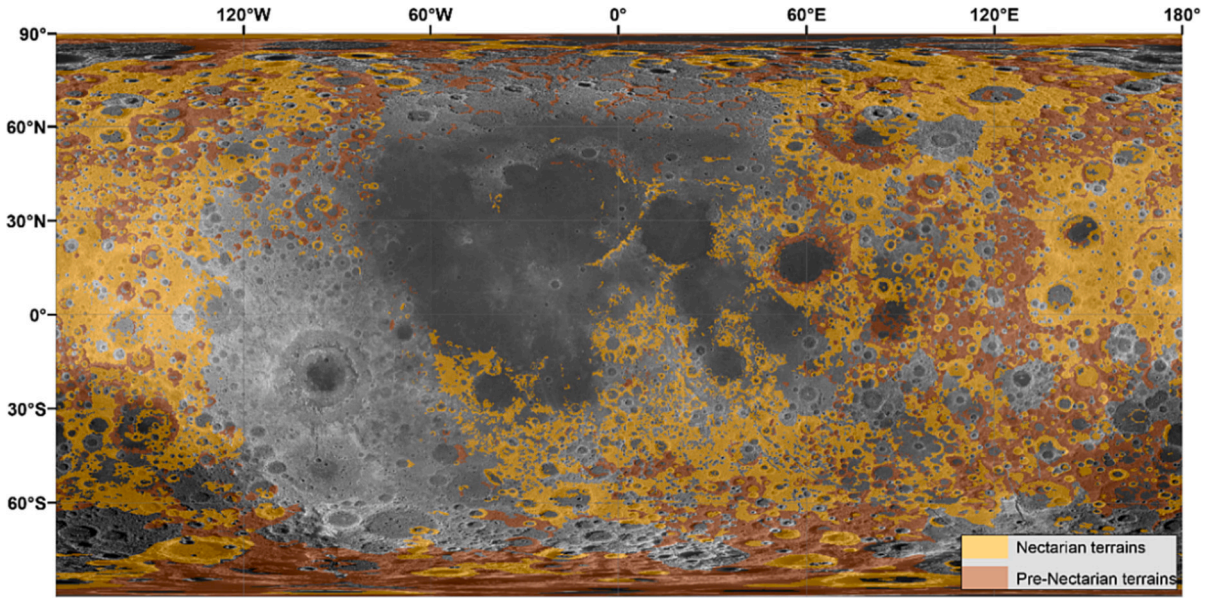

Fig. 9. Areas considered in the cratering density analysis. Nectarian (orange) and pre-Nectarian (brown) units selected from the lunar geological map (Fortezzo et al., 2020). Background: Lunar Reconnaissance Orbiter Wide Angle Camera (LRO-WAC) mosaic. (For interpretation of the references to colour in this figure legend, the reader is referred to the web version of this article.)

modified, leading to a relatively constant rate of large crater formation. However, our model may be inaccurate for periods beyond ~3.5 Ga due to the lack of calibration points and the change in the impactor population making the amplitude of the spatial variation of the cratering rate significantly different from that produced by the current NEO population.

Table 4
List of geological units (Fortezzo et al., 2020) selected in the crater density analysis.

Unit Age	Geological unit name	Symbol
Nectarian	Basin Undivided Unit	Nb
	Basin Lineated Unit	Nbl
	Basin Massif Unit	Nbm
	Crater Unit	Nc
	Nectaris Janssen Formation Unit	Nnj
	Plains Unit	Np
	Terra Unit	Nt
	Plains and Mantling, Terra Unit	Ntp
Pre-Nectarian	Basin Massif Unit	pNbm
	Basin Undivided Unit	pNb
	Crater Unit	pNc
	Terra Unit	pNt

Further sample collections at high latitudes, for example on the South Pole Aitken basin by NASA's Artemis mission, would allow testing the spatial variability of the lunar impact cratering rate over long timescales. More importantly, it will also provide additional constraints for the lunar chronology. The chronology model presented here for 0°N, 0°W is debiased from the spatial variation of the cratering rate and can thus be used to recalibrate the chronology systems of other terrestrial bodies. Orbital simulations of other inner planet's impactor population must be conducted to test the spatial dependency of the cratering rate on other worlds, along with the comparison with the cratering record to test its temporal validity.

Author contributions

A.L conceived the project and performed research, analyzed data, and wrote the paper. H.A.R.D. and P.V. provided critical feedback. D.R., M.G., P.P. and A.O. provided updated latitudinal impact distribution. P. M.S. investigated the gravitational focusing effect of the Earth in the lunar impact flux. J.H.F. provided crater data for the Chang'e-5 landing site. A.L., H.A.R.D., P.V., D.R., M.G., P.P., A.O., P.M.S., L.J., K.S., J.H.F., Y.Q. and G.K.B. contributed to the discussion and helped to shape the paper.

Code availability

The code converting model ages from the Neukum et al. (2001) chronology into the one we present here is available at: https://doi.org/10.5281/zenodo.10444295. We used the IDL 5.2 software (L3Harris geospatial https://www.l3harrisgeospatial.com/Software-Technology/IDL) to run the CraterStats II software available at https://www.geo.fu-berlin.de/en/geol/fachrichtungen/planet/software algorithm, the ESRI's ArcGIS 10.8.1 software suite (ESRI https://www.esri.com/en-us/arcgis/about-arcgis/overview) and Matlab (https://au.mathworks.com/products/matlab.html) to produce the analysis and the figures.

CRediT authorship contribution statement

Anthony Lagain: Conceptualization, Data curation, Formal analysis, Funding acquisition, Investigation, Methodology, Project administration, Supervision, Validation, Writing – original draft, Writing – review & editing. **Hadrien A.R. Devillepoix:** Investigation. **Pierre Vernazza:** Investigation. **Darrel Robertson:** Investigation, Resources. **Mikael Granvik:** Investigation, Resources. **Petr Pokorny:** Investigation, Resources. **Anthony Ozerov:** Investigation, Resources. **Patrick M. Shober:** Formal analysis, Investigation. **Laurent Jorda:** Investigation. **Konstantinos Servis:** Investigation. **John H. Fairweather:** Data curation, Investigation. **Yoann Quesnel:** Funding acquisition. **Gretchen K. Benedix:** Funding acquisition.

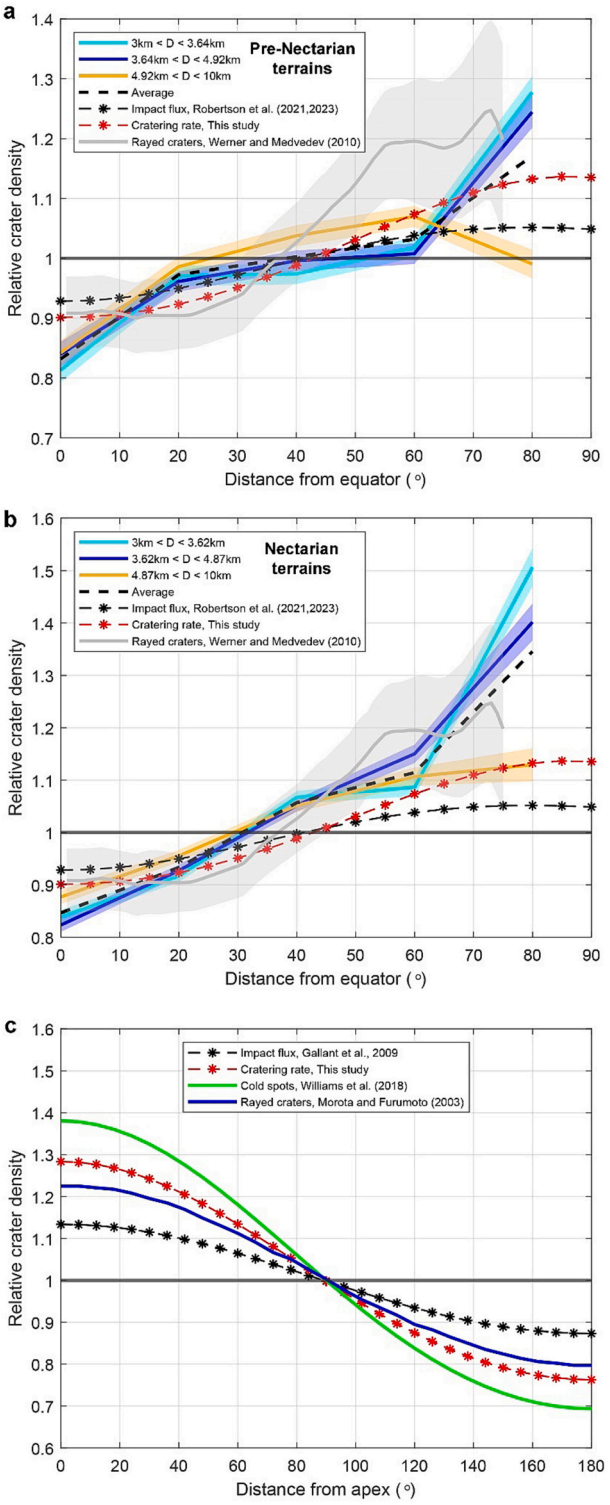

Fig. 10. Impact flux and cratering rate variabilities with respect to the distance from the equator and the apex compared to the cratering record. Cratering-density distribution on pre-Nectarian (panel a) and Nectarian terrains (panel b) with respect to the distance from the equator. The latitudinal distribution of rayed craters (Werner and Medvedev, 2010) is shown in grey. The relative density of cold spots (Williams et al., 2018) and rayed craters (Morota and Furumoto, 2003) with respect to the distance from the apex are shown in green and blue, respectively. The impact flux (black stars) and the relative cratering rate (red stars) models are shown on all panels for comparison. (For interpretation of the references to colour in this figure legend, the reader is referred to the web version of this article.)

Declaration of competing interest

The authors declare that they have no known competing financial interests or personal relationships that could have appeared to influence the work reported in this paper.

Data availability

The data that support the findings of this study are available within the paper and the relative cratering rate shown in Fig. 3 is available at: https://doi.org/10.5281/zenodo.10444295.

Acknowledgments

We thank an anonymous reviewer for providing insightful and constructive reviews that significantly improved the quality of this manuscript. Thanks are especially extended to Mikhail Kreslavsky for his helpful reviews and valuable suggestions, which played a crucial role in enhancing the overall quality of the manuscript. A.L., J.H.F. and G.K.B are funded by the Australian Research Council grants DP210100336, Curtin University, the Western Australian Government, and the Australian Government, and supported by the Pawsey Supercomputing Centre and ADACS (Astronomy Data and Compute Services). This work received support from the french government under the France 2030 investment plan, as part of the Initiative d'Excellence d'Aix-Marseille Université - A*MIDEX AMX-21-RID-O47. PP's work was supported by NASA Solar System Workings award 80NSSC21K0153, NASA SSERVI award 80NSSC19M0217, NASA ISFM EIMM award and the NASA Cooperative Agreement 80GSFC21M000. A.O.'s work was supported through NASA Cooperative Agreement 80NSSC19M0089. K.S. is supported by the Pawsey Supercomputing Centre, ADACS, and CSIRO.

Appendix A. Comparison between different lunar chronologies

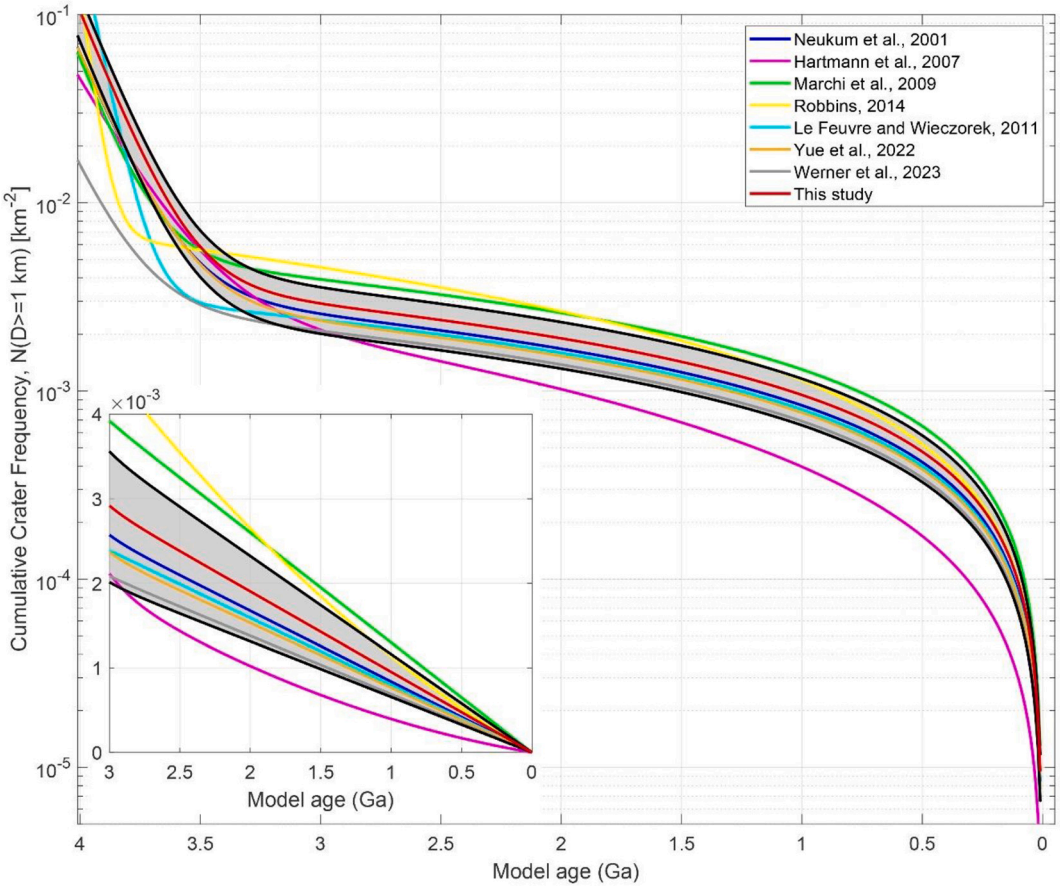

Fig. A.1. Comparison between different lunar crater chronologies (Neukum et al., 2001; Hartmann et al., 2007; Marchi et al., 2009; Robbins, 2014; Le Feuvre and Wieczorek, 2011 (valid at 0°N, 0°E) Yue et al., 2022 and Werner et al., 2023) and the chronology proposed in this study. The grey area corresponds to the range of possible chronology according to the model presented in this study (red curve), depending on the location of the considered area. Note that although Le Feuvre and Wieczorek (2011) proposed a spatially dependent chronology, its variability is not displayed for clarity. (For interpretation of the references to colour in this figure legend, the reader is referred to the web version of this article.)

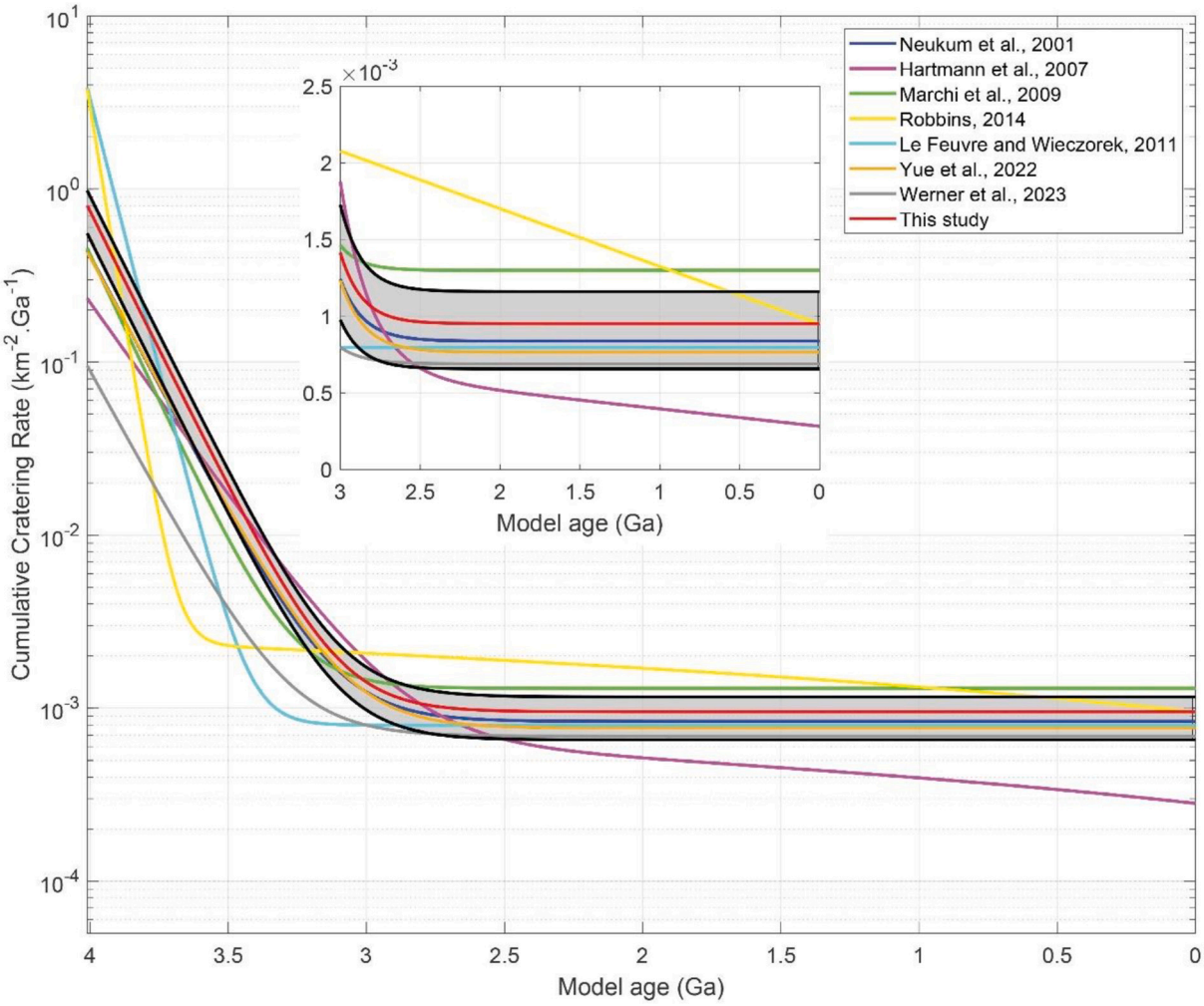

Fig. A.2. Cumulative cratering rate for different chronology models shown in Fig. A.1. The grey area corresponds to the range of possible cratering rate according to the model presented in this study (red curve), depending on the location of the considered area. (For interpretation of the references to colour in this figure legend, the reader is referred to the web version of this article.)

Appendix B. Impact craters model ages

Table B.1
Model age of lunar impact craters >50 km in diameter from Kirchoff et al. (2021) using the chronology system of [a]Marchi et al. (2009) and their equivalent using the Neukum's chronology[b] and the one presented in this study[c].

Crater	Latitude (°)	Longitude (°)	Model age[a]	Error	Model age[b]	Model age[c]
Kirkwood	68	−157	2.4	0.3	3.3	2.9
Jackson	22	−163	0.1	0.1	0.2	0.1
Morse	22	−175	3.5	0.2	3.5	3.5
Finsen	−42	−178	3.4	0.1	3.5	3.4
Vavilov	−1	−139	1.4	0.1	2.2	1.8
Robertson	21	−105	3.7	0.1	3.7	3.6
Ohm	18	−114	0.3	0.1	0.5	0.4
Leuschner	2	−109	1.5	0.1	2.3	1.8
Maunder	−15	−94	1.5	0.2	2.3	1.8
Hausen	−65	−89	3.4	0.2	3.5	3.4
Carpenter	70	−51	2.1	0.4	3.1	2.4
Pythagoras	64	−63	3.5	0.2	3.5	3.4
Cavalerius	5	−67	2.1	0.3	3.1	2.5
Zucchius	−61	−51	0.7	0.1	1.1	0.8
Philolaus	72	−33	0.8	0.1	1.2	0.9
Copernicus	10	−20	0.8	0.05	1.2	1.1
Bullialdus	−21	−22	3.7	0.1	3.7	3.6
Hainzel A	−40	−34	2	0.3	3	2.5
Anaxagoras	74	−10	0.3	0.1	0.5	0.4
Eratosthenes	15	−11	2.6	0.4	3.3	3.3
Tycho	−43	−11	0.09	0.02	0.1	0.1

(*continued on next page*)

Table B.1 (*continued*)

Crater	Latitude (°)	Longitude (°)	Model age[a]	Error	Model age[b]	Model age[c]
Moretus	−71	−6	3.8	0.1	3.8	3.7
Aristillus	34	1	1.6	0.2	2.5	2.3
Werner	−28	3	3.6	0.2	3.6	3.6
Scoresby	78	14	2.9	0.5	3.4	3.2
Aristoteles	50	17	2.2	0.4	3.2	3.0
Eudoxus	44	16	3.5	0.5	3.5	3.5
Hercules	47	39	2.5	0.7	3.3	3.3
Theophilus	−12	26	3	0.6	3.4	3.4
Fabricus	−43	42	2.2	0.3	3.2	3.2
Geminus	34	57	3.2	0.4	3.5	3.5
Taruntius	6	47	3.8	0.1	3.8	3.8
Langrenus	−9	61	3.6	0.2	3.6	3.6
Stevinus	−33	54	0.6	0.1	0.9	1.0
Hayn	64	84	1.7	0.2	2.6	2.4
Plutarch	24	79	2.1	0.4	3.1	3.3
Hamilton	−43	84	3.8	0.1	3.8	3.8
Moiseev	10	103	3.9	0.1	3.9	3.9
Olcott	21	118	3.4	0.3	3.5	3.5
King	5	121	0.5	0.2	0.8	1.0
Tsiolkovskiy	−20	129	2.6	0.6	3.3	3.4
Ricco	75	177	3.3	0.4	3.5	3.4
Sharonov	12	173	2.2	0.3	3.2	3.2
O'Day	−30	157	3.6	0.1	3.6	3.6
Birkeland	−30	174	3.8	0.1	3.8	3.7

Appendix C. Crater distribution analysis assumptions

The population of kilometer-scale craters on Nectarian and pre-Nectarian regions is controlled by both accumulation and retention (assumption #1). Crater retention in those densely cratered areas is also driven by cookie-cutting (Riedel et al., 2020), a geometric obliteration process implying the erasure of craters by the formation of new ones and causing large-scale resurfacing. Cratering analysis of pre-Nectarian terrains (Riedel et al., 2020) revealed that this process is dominant for the obliteration of complex craters, and that the degradation of simple craters is dominated by topographic diffusion (Craddock and Howard, 2000; Fassett and Thomson, 2014). In the case of a cookie cutting-dominated regime, areas subject to a higher flux would therefore experience more erasure driven by this process. Craters located in areas with higher impact flux would also experience an enhanced erasure in the case of a degradation regime controlled by topographic diffusion. Considering a spatially varying flux across the lunar surface, the crater retention would thus not be spatially homogeneous. However, the potential survival of the signal of a spatially varying cratering rate would necessarily imply that such erosional processes are not efficient enough in fully counteracting the signal of an enhanced impact flux.

Secondary craters lead to local overcratering areas, largely dominated by small craters, that are due to the fallback of ejecta on the surface forming radial crater chains, clusters or rays surrounding primary craters. Secondary craters are not recognized as such in the lunar crater database (Robbins, 2019). The most recent lunar geological map (Fortezzo et al., 2020) identifies major clusters of secondary craters. Although some isolated secondary crater clusters are omitted, discarding areas identified as contaminated by such craters would significantly reduce potential biases in the crater distribution analysis induced by the presence of these craters. Nevertheless, the contribution of basin secondaries, including those from Orientale, are expected to be >3 km, and some might not have been recognized as such on the geological map we use. The identification of such secondaries in the considered population would require a large survey of morphological characteristics of individual craters contained in the database and is beyond the scope of this study. The crater-size frequency distribution of secondary craters exhibits a steeper slope than that of primary craters (Lagain et al., 2021b, 2021c; Robbins and Hynek, 2011) and their lifetime on planetary surfaces is shorter than that of primary craters due to a lower depth-diameter ratio (Lagain et al., 2021b). Limiting our study to the analysis of large (3–10 km) craters on old surfaces would therefore limit (but not annihilate) the influence of areas highly contaminated by secondary craters, not recognized as such in crater databases or geological maps (assumption #2).

If the density of craters reaches a steady state, or a saturation equilibrium, the surface history beyond a certain time horizon is lost (Hartmann, 1984; Xiao and Werner, 2015). For a region receiving higher impact flux, this horizon moves closer, but is impossible to determine using crater density alone because after sufficient time, all surfaces will exhibit the same final cratering distribution for any impact flux. Possible saturation state for craters smaller than ~7 km on some lunar pre-Nectarian highlands has been previously reported (Robbins, 2019; Xiao and Werner, 2015). However, some lunar terrains where craters >40 km reach >10% geometric saturation are not in equilibrium state (Povilaitis et al., 2018), although such a level of saturation is commonly considered to reflect a crater population in equilibrium (Xiao and Werner, 2015). Richardson and Abramov (2020) argued that lunar highlands reached the equilibrium for craters smaller than 250 km in diameter. This variety of results illustrate that an arbitrary level of saturation cannot be used to conclude that the cratering has reached equilibrium because the degradation process depends on crater size (Riedel et al., 2020; Fassett and Thomson, 2014; Povilaitis et al., 2018). If the whole population of craters analyzed here would be in equilibrium, and if the retention of craters is homogeneous across analyzed surfaces (assumption #1), the crater density signal should not show any significant spatial variations, or at least should not correlate with the NEO impact probabilities. Therefore, any correlation between the signal of the crater distribution on both terrain types (pre-Nectarian and Nectarian) for different size ranges and the NEO impact probabilities is unlikely to originate from saturation equilibrium state (assumption #3).

One could argue that TPW and long-term/high amplitude obliquity variations might also play a role in the latitudinal crater distribution. Although TPWs of a few degrees have been proposed for the Moon (Siegler et al., 2016), they most likely occurred in ancient time, for which a very limited number of small craters (<5 km) still visible at the surface were formed prior to this period compared to large craters (>20 km). In addition, recent investigation on the contribution of craters and basins in the lunar gravitational figure (Smith et al., 2022) suggests that the Moon's rotational pole has not moved over the last 3.8 Ga by >2° in latitudes. In parallel, the evolution of the Moon's obliquity is poorly constrained over geological time, but thought to be relatively stable, close to 0°, over the last ~4 Ga (Le Feuvre and Wieczorek, 2011; Ćuk et al., 2016). The comparison of the cratering

density over different latitudinal ranges and for different crater sizes (those smaller than 20 km, mostly formed after potential TPWs) mitigate this potential source of bias. We therefore neglect both TPW and long-term high obliquity excursion in the crater distribution over areas analyzed here because the amplitude of both effects can only attenuate and not make disappear potential latitudinal fluctuation of the cratering density induced by a flux varying sufficiently in latitudes (assumption #4).

Appendix D. Crater density analysis

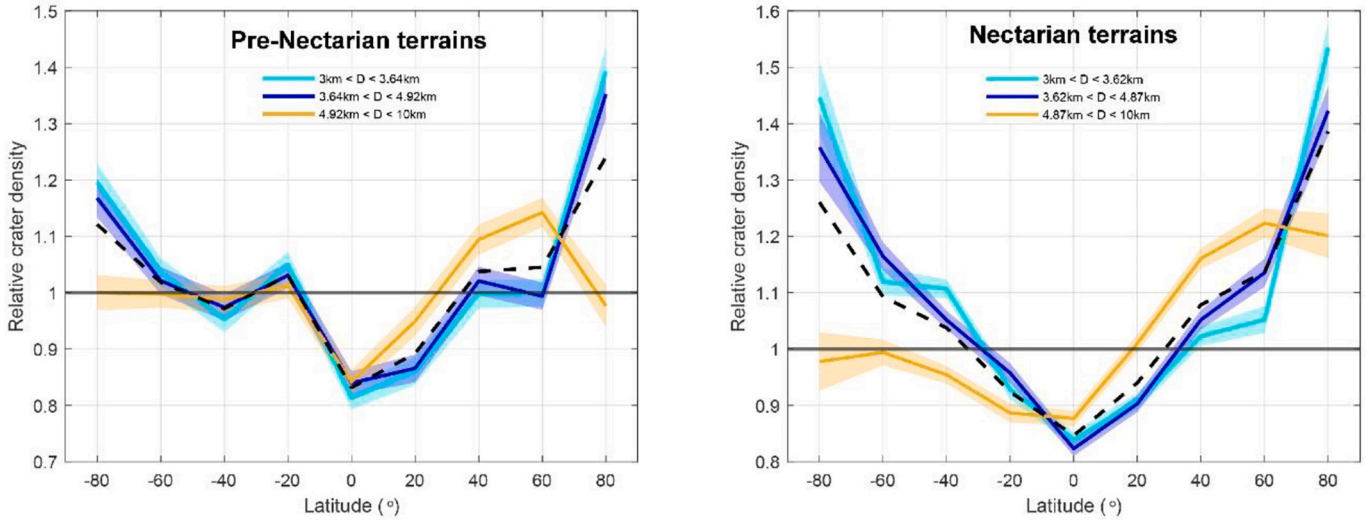

Fig. D.1. Relative crater density variation with respect to the latitude on pre-Nectarian and Nectarian terrains (left and right panels, respectively). The density is computed over 20° latitudinal bands.

Table D.1
Results of the longitudinal crater density analysis on pre-Nectarian terrains. The apex/antapex ratios are computed using the average of the two first and last longitudinal bins. The relative density of cold spots reported by [a]Williams et al. (2018) and that of rayed craters from [b]Morota and Furumoto, 2003are also given.

Distance from apex (°)	Relative crater density from cold spots[a]	Relative crater density from rayed craters[b]	Cratering rate, this study
0	1.38	1.23	1.28
20	1.36	1.21	1.26
40	1.28	1.17	1.21
60	1.18	1.11	1.13
80	1.06	1.04	1.04
100	0.94	0.96	0.95
120	0.84	0.89	0.87
140	0.76	0.85	0.81
160	0.71	0.81	0.78
180	0.69	0.80	0.76
Apex/Antapex Ratio	1.95	1.52	1.68

Table D.2
Results of the latitudinal crater density analysis on pre-Nectarian terrains. The pole/equator ratios are computed using the average of the two first and last latitudinal bins. The relative density of rayed craters reported by [a]Werner and Medvedev (2010) is also given.

Distance from equator (°)	Latitude range (°)	Area (x10^6 km^2)	Relative crater density and errors for each size bin						Cratering rate from rayed craters[a]	Cratering rate, This study
			3 km – 3.62 km		3.62 km – 4.87 km		4.87 km – 10 km			
0	[−10 10]	0.95	0.81	0.02	0.84	0.02	0.84	0.02	0.91	0.90
20	[−30 −10]; [10 30]	1.69	0.97	0.02	0.96	0.02	0.99	0.02	0.90	0.92
40	[−50 −30];[30 50]	1.66	0.97	0.02	1.00	0.02	1.04	0.02	1.03	0.99
60	[−70 −50];[50 70]	1.71	1.02	0.02	1.01	0.02	1.07	0.02	1.27	1.07
80	[−90 −70];[70 90]	0.86	1.28	0.03	1.24	0.03	0.99	0.02	NaN	1.13
Pole/Equateur Ratio			1.29		1.25		1.13		1.40	1.26

References

Archinal, B.A., et al., 2015. Report of the IAU working group on cartographic coordinates and rotational elements: celestial. Mech. Dynam. Astronom. 130, 22. https://doi.org/10.1007/s10569-017-9805-5.

Benedix, G.K., et al., 2020. Deriving surface ages on Mars using automated crater counting. ESS 7 (3). https://doi.org/10.1029/2019EA001005.

Bottke, W.F., et al., 2002. Debiased orbital and size distributions of the near-Earth objects. Icarus 156, 399–433. https://doi.org/10.1006/icar.2001.6788.

Bottke, W.F., et al., 2007. An asteroid breakup 160 Myr ago as the probable source of the K/T impactor. Nature 449, 06070. https://doi.org/10.1038/nature06070.

Bottke, W.F., et al., 2015. The collisional evolution of the asteroid belt. In: Michel, P., DeMeo, F., Bottke, W.F. (Eds.), Asteroids IV. U. Arizona Press, pp. 701–724. https://doi.org/10.2458/azu_uapress_9780816532131-ch036.

Carr, M.H., Head III, J.W., 2010. Geologic history of Mars. Earth Planet. Sci. Lett. 294, 185–203. https://doi.org/10.1016/j.epsl.2009.06.042.

Carry, B., 2012. Density of asteroids. Planet. Space Sci. 73, 98–118. https://doi.org/10.1016/j.pss.2012.03.009.

Collins, G.S., et al., 2005. Earth impact effects program: a web-based computer program for calculating the regional environmental consequences of a meteoroid impact on Earth. Meteorit. Planet. Sci. 40, 817–840. https://doi.org/10.1111/j.1945-5100.2005.tb00157.x.

Craddock, R.A., Howard, A.D., 2000. Simulated degradation of lunar impact craters and a new method for age dating farside mare deposits. JGR 105, 20387–20402. https://doi.org/10.1029/1999JE001099.

Ćuk, M., et al., 2016. Tidal evolution of the Moon from a high-obliquity, high-angular-momentum Earth. Nature 539, 402–406. https://doi.org/10.1038/nature19846.

Fairweather, J.H., et al., 2022. Automatic mapping of small lunar impact craters using LRO-NAC images. ESS 9. https://doi.org/10.1029/2021EA002177 e2021EA002177.

Fairweather, J.H., et al., 2023. Lunar surface model age derivation: comparisons between automatic and human crater counting using LRO-NAC and Kaguya TC images. Earth Space Sci. 10 (7) https://doi.org/10.1029/2023EA002865 e2023EA002865.

Farhat, M., et al., 2022. The resonant tidal evolution of the Earth-Moon distance. A&A 665, L1. https://doi.org/10.1051/0004-6361/202243445.

Fassett, C.I., 2016. Analysis of impact crater populations and the geochronology of planetary surfaces in the inner solar system. JGR: Planets 121, 1900–1926. https://doi.org/10.1002/2016JE005094.

Fassett, C.I., Thomson, B.J., 2014. Crater degradation on the lunar maria: topographic diffusion and the rate of erosion on the Moon. JGR: Planets 119, 2255–2271. https://doi.org/10.1002/2014JE004698.

Fortezzo, C.M., et al., 2020. Release of the Digital Unified Global Geologic Map of the Moon At 1:5,000,000- Scale. 51st LPSC. https://www.hou.usra.edu/meetings/lpsc2020/pdf/2760.pdf.

Fujiwara, A., et al., 2006. The rubble-pile asteroid Itokawa as observed by Hayabusa. Science 312, 1330–1334. https://doi.org/10.1126/science.1125841.

Gallant, J., et al., 2009. Current bombardment of the earth-moon system: emphasis on cratering asymmetries. Icarus 202 (2), 371–382. https://doi.org/10.1016/j.icarus.2009.03.025.

Giguere, T.A., et al., 2022. Lava flow ages in northeastern Oceanus Procellarum: the need for calibrating crater counting procedures. Icarus 375, 114838. https://doi.org/10.1016/j.icarus.2021.114838.

Granvik, M., et al., 2018. Debiased orbit and absolute-magnitude distributions for near-Earth objects. Icarus 312, 181–207. https://doi.org/10.1016/j.icarus.2018.04.018.

Hartmann, W.K., 1984. Does crater “saturation equilibrium” occur in the solar system? Icarus 60, 56–74. https://doi.org/10.1016/0019-1035(84)90138-6.

Hartmann, W.K., Neukum, G., 2001. Cratering chronology and the evolution of Mars. Space. Sci. Rev. 96, 165–194. https://doi.org/10.1023/A:1011945222010.

Hartmann, W.K., et al., 2007. Possible long-term decline in impact rates 2. Lunar impact-melt data regarding impact history. Icarus 186, 11–23. https://doi.org/10.1016/j.icarus.2006.09.009.

Haruyama, J., et al., 2008. Planned radiometrically calibrated and geometrically corrected products of lunar high-resolution terrain camera on SELENE. Adv. Space Res. 42 (2), 310–316. https://doi.org/10.1016/j.asr.2007.04.062.

Hiesinger, H., et al., 2003. Ages and stratigraphy of mare basalts in Oceanus Procellarum, Mare Nubium, Mare Cognitum, and Mare Insularum. JGR 108, 5065. https://doi.org/10.1029/2002JE001985.

Hiesinger, H., et al., 2012. How old are young lunar craters? JGR: Planets 117, E00H10. https://doi.org/10.1029/2011JE003935.

Jia, M., et al., 2020. A catalogue of impact craters larger than 200 m and surface age analysis in the Chang’e-5 landing area. EPSL 541, 116272. https://doi.org/10.1016/j.epsl.2020.116272.

Kawamura, T., et al., 2011. Cratering asymmetry on the moon: new insight from the Apollo passive seismic experiment. GRL 38, L15201. https://doi.org/10.1029/2011GL048047.

Kirchoff, M.R., et al., 2021. Suggestion that recent (≤3 Ga) flux of kilometer and larger impactors in the Earth-Moon system has not been constant. Icarus 114110. https://doi.org/10.1016/j.icarus.2020.114110.

Kreslavsky, M., et al., 2012. New Observational Evidence of Nonuniform Cratering of the Moon, LPSC 43, #1193. https://www.lpi.usra.edu/meetings/lpsc2012/pdf/1193.pdf.

Lagain, A., et al., 2020. Impact cratering rate consistency test from ages of layered ejecta on Mars. Planet. Space Sci. 180, 104755 https://doi.org/10.1016/j.pss.2019.104755.

Lagain, A., et al., 2021a. Model age derivation of large Martian impact craters, using automatic crater counting methods. Earth Space Sci. 8 https://doi.org/10.1029/2020EA001598 e2020EA001598.

Lagain, A., et al., 2021b. The Tharsis mantle source of depleted shergottites revealed by 90 million impact craters. Nat. Commun. 12, 6352. https://doi.org/10.1038/s41467-021-26648-3.

Lagain, A., et al., 2021c. Mars crater database: a participative project for the classification of the morphological characteristics of large Martian craters. In: Large Meteorite Impacts and Planetary Evolution VI, Wolf Uwe Reimold, Christian Koeberl. https://doi.org/10.1130/2021.2550(29).

Lagain, A., et al., 2022. Has the impact flux of small and large asteroids varied through time on Mars, the Earth and the Moon? EPSL 579, 117362. https://doi.org/10.1016/j.epsl.2021.117362.

Le Feuvre, M., Wieczorek, M.A., 2008. Nonuniform cratering of the terrestrial planets. Icarus 197 (1), 291–306. https://doi.org/10.1016/j.icarus.2008.04.011.

Le Feuvre, M., Wieczorek, M.A., 2011. Nonuniform cratering of the moon and a revised crater chronology of the inner solar system. Icarus 214 (1), 1–20. https://doi.org/10.1016/j.icarus.2011.03.010.

Li, Q.L., et al., 2021. Two-billion-year-old volcanism on the Moon from Chang’e-5 basalts. Nature 600, 54–58. https://doi.org/10.1038/s41586-021-04100-2.

Marchi, S., et al., 2009. A new chronology for the Moon and Mercury. Astron. J. 137, 4936–4948. https://doi.org/10.1088/0004-6256/137/6/4936.

Mazrouei, S., et al., 2019. Earth and Moon impact flux increased at the end of the Paleozoic. Science 363, 253–257. https://doi.org/10.1126/science.aar4058.

Michael, G.G., Neukum, G., 2010. Planetary surface dating from crater size–frequency distribution measurements: partial resurfacing events and statistical age uncertainty. EPSL 294 (3–4), 223–229. https://doi.org/10.1016/j.epsl.2009.12.041.

Minton, D.A., et al., 2019. The equilibrium size-frequency distribution of small craters reveals the effects of distal ejecta on lunar landscape morphology. Icarus 326, 63–87. https://doi.org/10.1016/j.icarus.2019.02.021.

Morbidelli, A., et al., 2018. The timeline of the lunar bombardment: revisited. Icarus 305, 262–276. https://doi.org/10.1016/j.icarus.2017.12.046.

Morota, T., Furumoto, M., 2003. Asymmetrical distribution of rayed craters on the Moon. EPSL 206 (3–4), 315–323. https://doi.org/10.1016/S0012-821X(02)01111-1.

Morota, T., et al., 2005. Influence of the asymmetrical cratering rate on the lunar chronology. Icarus 173, 322–324. https://doi.org/10.1016/j.icarus.2004.08.016.

Morota, T., et al., 2011. Timing and characteristics of the latest mare eruption on the Moon. EPSL 302, 255–266. https://doi.org/10.1016/j.epsl.2010.12.028.

Nesvorný, D., et al., 2017. Modeling the historical flux of planetary impactors. Astron. J. 153, 103. https://doi.org/10.3847/1538-3881/153/3/103.

Nesvorný, D., et al., 2022. Formation of lunar basins from impacts of leftover planetesimals. ApJL 941, L9. https://doi.org/10.3847/2041-8213/aca40e.

Neukum, G., 1983. NASA Technical Memorandum TM-77558 153. https://ntrs.nasa.gov/api/citations/19840027189/downloads/19840027189.pdf.

Neukum, G., et al., 2001. Cratering records in the inner solar system in relation to the lunar reference system. Space Sci. Rev. 96, 55–86. https://doi.org/10.1023/A:1011989004263.

Norman, M.D., 2009. The lunar cataclysm: reality or ‘mythconception’? Elements 5 (1), 23–28. https://doi.org/10.2113/gselements.5.1.23.

Pokorný, P., Vokrouhlický, D., 2013. Opik-type collision probability for high-inclination orbits: targets on eccentric orbits. Icarus 226, 682. https://doi.org/10.1016/j.icarus.2013.06.015.

Povilaitis, R.Z., et al., 2018. Crater density differences: exploring regional resurfacing, secondary crater populations, and crater saturation equilibrium on the Moon. PSS 162, 41–51. https://doi.org/10.1016/j.pss.2017.05.006.

Qian, Y.Q., et al., 2018. Geology and scientific significance of the Rümker region in northern Oceanus Procellarum: China’s Chang’E-5 landing region. JGR: Planets 123, 1407–1430. https://doi.org/10.1029/2018JE005595.

Qian, Y.Q., et al., 2021. Young lunar mare basalts in the Chang’e-5 sample return region, northern Oceanus Procellarum. EPSL 555, 116702. https://doi.org/10.1016/j.epsl.2020.116702.

Rein, H., Liu, S.-F., 2012. REBOUND: an open-source multi-purpose N-body code for collisional dynamics. A&A 537, A128. https://doi.org/10.1051/0004-6361/201118085.

Rein, H., Tamayo, D., 2015. WHFAST: a fast and unbiased implementation of a symplectic Wisdom–Holman integrator for long-term gravitational simulations. Mon. Not. R. Astron. Soc. 452 (1), 376–388. https://doi.org/10.1093/mnras/stv1257.

Richardson, J.E., Abramov, O., 2020. Modeling the formation of the lunar upper megaregolith layer. Planet. Sci. J. 1, 2. https://doi.org/10.3847/PSJ/ab7235.

Riedel, C., et al., 2020. Degradation of small simple and large complex lunar craters: not a simple scale dependence. J. Geophys. Res. Planets 125. https://doi.org/10.1029/2019JE006273 e2019JE006273.

Robbins, S.J., 2014. New crater calibrations for the lunar crater-age chronology. EPSL 403, 188–198. https://doi.org/10.1016/j.epsl.2014.06.038.

Robbins, S.J., 2019. A new global database of lunar impact craters >1–2 km: 1. Crater locations and sizes, comparisons with published databases, and global analysis. JGR: Planets 124, 871–892. https://doi.org/10.1029/2018JE005592.

Robbins, S.J., Hynek, B.M., 2011. Secondary crater fields from 24 large primary craters on Mars: insights into nearby secondary crater production. JGR 116, E10003. https://doi.org/10.1029/2011JE003820.

Robertson, D., et al., 2021. Latitude variation of flux and impact angle of asteroid collisions with Earth and the Moon. Planet. Sci. J. 2, 88. https://doi.org/10.3847/PSJ/abefda.

Robertson, D., et al., 2023. Erratum: “latitude variation of flux and impact angle of asteroid collisions with Earth and the Moon”. (2021, Planetary Science Journal, 2, 88). Planet. Sci. J. 4, 19. https://doi.org/10.3847/PSJ/aca1a7.

Siegler, M., et al., 2016. Lunar true polar wander inferred from polar hydrogen. Nature 531, 480–484. https://doi.org/10.1038/nature17166.

Smith, D.E., et al., 2022. The contribution of small impact craters to lunar polar wander. Planet. Sci. J. 3 (9) https://doi.org/10.3847/PSJ/ac8c39.
Stöffler, D., Ryder, G., 2001. Stratigraphy and isotope ages of lunar geologic units: chronological standard for the inner solar system. Space Sci. Rev. 96 (1/4), 9–54. https://doi.org/10.1023/A:1011937020193.
Wang, N., Zhou, J.-L., 2016. Analytical formulation of lunar cratering asymmetries. A&A 594, A52. https://doi.org/10.1051/0004-6361/201628598.
Werner, S.C., Medvedev, S., 2010. The lunar rayed-crater population - characteristics of the spatial distribution and ray retention. EPSL 295 (1–2), 147–158. https://doi.org/10.1016/j.epsl.2010.03.036.
Werner, S.C., et al., 2023. Review and revision of the lunar cratering chronology - lunar timescale part 2. Planet. Sci. J. 4, 147. https://doi.org/10.3847/PSJ/acdc16.
Williams, J.-P., et al., 2018. Lunar cold spots and crater production on the moon. JGR: Planets 123, 2380–2392. https://doi.org/10.1029/2018JE005652.
Wu, B., et al., 2018. Rock abundance and crater density in the candidate Chang'E-5 landing region on the moon. JGR: Planets 123, 3256–3272. https://doi.org/10.1029/2018JE005820.
Xiao, Z., Werner, S.C., 2015. Size-frequency distribution of crater populations in equilibrium on the Moon. JGR: Planets 120, 2277–2292. https://doi.org/10.1002/2015JE004860.
Xie, M., et al., 2021. Change in the Earth-Moon impactor population at about 3.5 billion years ago. Nat. Astron. 5, 128–133. https://doi.org/10.1038/s41550-020-01241-8.
Yue, Z., et al., 2022. Updated lunar cratering chronology model with the radiometric age of Chang'e-5 samples. Nat. Astron. 6, 541–545. https://doi.org/10.1038/s41550-022-01604-3.
Zahnle, K., et al., 2001. Differential cratering of synchronously rotating satellites by ecliptic comets. Icarus 153 (1), 111–129. https://doi.org/10.1006/icar.2001.6668.